Edvard Stubberud

Intermittent dynamics in dense active matter

Master’s thesis in Applied Physics and Mathematics
Supervisor: Paul Gunnar Dommersnes
June 2020

Master’s thesis

NTNU
Norwegian University of Science and Technology
Faculty of Natural Sciences
Department of Physics

NTNU
Norwegian University of
Science and Technology

Edvard Stubberud

Intermittent dynamics in dense active matter

Master's thesis in Applied Physics and Mathematics
Supervisor: Paul Gunnar Dommersnes
June 2020

Norwegian University of Science and Technology
Faculty of Natural Sciences
Department of Physics

NTNU
Norwegian University of
Science and Technology

Summary

Active-matter physics is concerned with modeling and understanding the collective behaviour of all scales of life, from swimming bacteria to animals in flocks. This study examines a system of self-propelled particles, a type of Langevin dynamic, often used to describe active-matter systems. The equations of motion for active matter systems were derived, particularly including periodic boundary conditions, a stochastic rotational diffusion term, soft particle-particle interactions, and a particle-particle torque similar to the classical XY-model, known from ferromagnetic alignment in statistical mechanics. The results of the study are generated by numerical computations of a two dimensional system.

In disordered systems, such as glasses and jammed granular matter, various correlation functions are used to characterize the systems, including the four-point susceptibility function, the kurtosis of the energy and the energy distribution of the system. In this thesis, these functions are used to analyze the numerical results. The results show that the system without particle-particle torque, transitions from an active crystal to an active liquid crystal when the self-propulsion velocity is increased above the critical point. The phase transition observed has similarities to a glass-like transition. The transition occurs at the critical point of the system dynamics, where self-propulsion forces overcomes the repulsive particle-particle interactions. At the critical point of the system, the energy distribution of the system follows the Gutenberg-Richter law. This is a main result of the study. Intermittency events in forms of avalanches are observed, where the frequency and energy magnitudes increase with the self-propulsion velocity. The avalanches consists of a collective motion of a small local ensembles of particles, while the rest of the particles in the system are at dynamical arrest.

Including nematic particle-particle alignment, the system studied exhibits spontaneous symmetry breaking, similar to the Vicsek model, and global ordering can be observed in the two dimensional system. Furthermore, the system has a long transient behaviour before the ordered steady state is reached. Finally, the self-propulsion velocity dependence of the ordered system shows similarities to the phase transition of the system without particle-particle torque. The results obtained can be relevant to explain the collective dynamics of migrating epithelial cells or tumor cells in dense tissues.

Sammendrag

**Aktiv-materie fysikk bruker teoretiske modeller for å forstå og forklare kollektiv oppførsel for livsformer av alle størrelser, fra svømmende bakterier til dyr i flokk. Dette studiet utforsker et system med selvdrivende partikler, en form for Langevin dynamikk, ofte brukt til å beskrive aktiv-materie fysikk. Bevegelsesligningene for aktive-materie systemer har blitt derivert, som inkluderer periodiske grensebetingelser, en stokastisk rotasjonsdiffusjonkoeffisient, myk partikkel-partikkel-vekselvirkning, og et partikkel-partikkel-dreiemoment, lignende den klassiske XY-modellen, gjenkjennbar fra ferromagnetisk innretning i statisk mekanikk. Resultatet av dette studiet er generert ved numeriske beregninger av et todimensjonalt system.

I uordnede systemer, slik som glass og fastkjørte granulære systemer, brukes forskjellige korrelasjonsfunksjonen til å karatereise systemer, slik for fire-punkts susceptibilitetsfunksjonen, kurtosen av energien og energifordelingen i systemet. In denne avhandlingen blir disse funksjonene blir brukt til å analysere de numeriske resultatene. Resultatene viser at systemet, uten partikkel-partikkel-dreiemoment, har en overgang fra en aktiv krystall til en aktiv flytende krystall når den selvdrivende hastigheten økes over det kritiske punktet. Den observerte faseovergangen har likheter med en glass-lignende overgang. Overgangen foregår på det kritiske punktet i dynamikken til systemet, hvor den selvdrivende karften blir større enn partikkel-partikkel-interaksjonen. Hovedresultatet i dette studiet kan observeres ved det kritiske punktet i systemet, hvor distribusjonen av energier i systemet følger Gutenberg-Richter loven. Denne typen skaleringslov er en relativt ny observasjon innen aktiv-materie fysikk. Bruddhendelser i form av skred kan observeres, hvor hyppigheten og omfanget til energien øker med den selvdrivende hastigheten. Skredene består av kollektive bevegelser in små grupperinger av partikler, hvor resten av partiklene i systemet forblir i ro.

Ved å inkludere nematisk partikkel-partikkel-innretning, viser system spontane symmetribrudd, lignende observasjonene i Vicsek modellen, og global innordning kan observeres i todimensjonale systemer. Videre, observeres det at systemet har en lang transient oppførsel, før det når en stabil tilstand. Til slutt, for det høyt innordnede systemet, fremstår avhengige av den selvdrivende hastigheten lik faseovergangen i systemet uten partikkel-partikkel-innretning. Resultatene oppnådd kan være relevante for å forklare kollektiv dynamikk i hudceller eller kreftceller i vev.

Preface

This Master's thesis is the finale chapter of my Master of Science degree (Sivilingeniør), at the Norwegian University of Science and Technology (NTNU) for the Department of Physics. It concludes my five years integrated degree in Applied Physics and Mathematics, with a specialization within Applied Physics.

I want to give a great thanks to my supervisor, Professor Paul Gunnar Dommersnes, whom guided me through my work on this thesis. His many and long discussion with me have given me an inspiring and educational last 10 months at my time at NTNU. He has challenged me to explore topics far beyond my reach of knowledge, and filled in gaps in my understanding of physics. Further I also want to give a thanks to the STEAM team at CERN for opening my eyes to numerical physics, thorough my technical student internship there.

Furthermore, I would also like to thank all my fellow students and close friends at the study Applied Physics and Mathematics, who without, the last five years of my life would never have been as fun and educational. Lastly, I would like to thank my parents for the unconditional support and motivation through all my 18 years of education, and helping me with the final touches of my thesis.

Table of Contents

Summary **i**

Sammendrag - (Summary in Norwegian) **ii**

Preface **iii**

Table of Contents **vi**

List of Tables **vii**

List of Figures **xii**

1 Introduction **1**

2 Theory **5**
- 2.1 The Vicsek model 5
- 2.2 Langevin equation 6
- 2.3 Active Brownian dynamics 6
  - 2.3.1 Expectation values of free active Brownian particles 8
- 2.4 System boundary conditions 9
  - 2.4.1 Periodic boundary conditions 10
- 2.5 Particle-particle interaction 11
  - 2.5.1 Weeks-Chandler-Andersen potential 12
  - 2.5.2 Harmonic interaction potential 13
  - 2.5.3 Particle radius 14
  - 2.5.4 Packing fraction 14
  - 2.5.5 Alignment torque with the XY-model 15
- 2.6 Collective motion in confinement 17
- 2.7 Spontaneous symmetry breaking 18
- 2.8 Four-point susceptibility function 19
  - 2.8.1 Self-overlap order parameter 20

  2.9 Particle energy 21
    2.9.1 Interaction energy 21
    2.9.2 Kinetic energy 21
    2.9.3 Kurtosis of the kinetic energy 22
  2.10 Crackling noise and Gutenberg-Richter law 23
  2.11 States of active matter systems 23
    2.11.1 Solid 24
    2.11.2 Jamming 26
    2.11.3 Liquid 27
    2.11.4 Intermittency 27

3 Numerical Methods **29**
  3.1 Discretization 29
    3.1.1 Integrating the equations of motion for a free particle 29
    3.1.2 Boundary conditions and particle-particle interaction 30
    3.1.3 Adams-Bashforth integration for equations of motion 30
    3.1.4 Uniform probability distribution 31
    3.1.5 Derived quantities 31
    3.1.6 Initialization of system 32
  3.2 Numerical implementation 32

4 Results and Discussion **35**
  4.1 System setup 35
  4.2 Simulation results 36
    4.2.1 Simulations with particle-particle force 38
    4.2.2 Simulations with particle-particle force and nematic torque 52

5 Conclusion **61**
  5.1 Current simulations and future directions 61
  5.2 Further development of simulation tool 63

Bibliography **65**

A Validation of simulation program **71**
  A.1 Optimization of time steps for integration schemes 71
  A.2 Sedimentation in infinite potential well 72
    A.2.1 Simulations of particle sedimentation 73

List of Tables

4.1 Free variables in the physical model for an active matter system with periodic boundary conditions, harmonic potential for the particle-particle force and the flying XY-model for the particle-particle torque. The values denoted in the third column is assumed for all following simulations and the notation ”-” implies the variable will be varied in the results. 35

4.2 Free variables in the simulation program for the active matter system. The values correspond to a high packing fraction. 36

List of Figures

1.1 Biological active matter. (a) shows a school of fish in circular orientational ordered vortex state. (b) shows Epithelial tissue of Madine–Darby canine kidney cells. (c) shows the Escherichia coli bacteria grown on agarose. (d) shows a illustration of polar and apolar active particles exhibiting polar and nematic order. 2

2.1 Illustration of a particle interacting with a boundary. The force is denoted as $\vec{F}_{\mathrm{b}}$ and the torque as Γ_{b}, as in Equations (2.19) and (2.20), respectively. 10

2.2 Illustration of particle-particle interaction for two particles. The interparticle forces are denoted as $\vec{F}_{\mathrm{pp}}$ and torques as Γ_{pp}, as in Equations (2.22) and (2.23), respectively. 12

2.3 Sketch of the time behavior $\chi_4(t)$, for different time regimes, derived from from mode coupling theory close to the glass transition temperature. Figure reused from [1]. 20

2.4 Gutenberg-Richter law for earthquakes measured in 1995. (a) shows the energy of earthquakes as a function of time. The energy distribution is discrete as typical for crackling noise. Some extremely high energies can be seen. (b) shows a linear decay of energies in the log-log space, as formulated by the Gutenberg-Richter law. 24

2.5 Active crystal under scanning electron microscopy. (A) A single bimaterial colloid. (B) Living crystals assembled from a homogeneous distribution (inset) under illumination by blue light. (C) Living crystals melt by thermal diffusion when the light is turned off, show for 10 s (inset, 100 s) after the light is turned off. 25

2.6 Observed partly jamming in epithelial tissue. (a) shows a picture of the tissue under a microscope. (b) depicts the velocities of each tissue cell as arrows. The gray area represents (or at least close to) dynamical arrest. . . 26

4.1 Snapshots of the particles at $t = 25$ with periodic boundaries. The left side shows the whole system, while the right side show the area marked in white. The color bar and the arrows indicate the orientation of the particle. The color bar range from $-\pi$ to π, and represent the polar angel of the particles. The particle size in not necessarily up to scale. 37

4.2 Derived values of simulation with $\gamma = 0.0$, i.e. no directional alignment, with the simulations parameters in Table 4.2. (a) The order parameter $Q_t(\tau)$ shows a clear relation between the self-propulsion velocity and decorrelation of particle overlap. (b) The four-point susceptibility function $\chi_4(\tau)$ shows a large increase in the variance of the self-overlap function as u_0 approaches 0.4 from below, which indicates a change in behaviour of the system. In (c) the self-propulsion values of u_0 = 0.2, 0.3, 0.4 the kurtosis $\kappa(\tau)$ exhibits large changes with with increasing time τ. 39

4.3 Values derived from Figure 4.2. (a) The four-point susceptibility function from Figure 4.2b, for the x-axis rescaled to $u_0\tau$, where a clear data collapse is visible for small values of the self-propulsion velocity. (b) $\kappa_{\text{ex}}(\tau = 0+)$ where 0+ is the smallest store time interval which is $50\Delta t$. A point of inflection can be found between 0.4 and 0.5. if the data point of 0.2 is disregarded. 41

4.4 Several representations of the calculated normalized kinetic energy of the system in Figure 4.2 for $u_0 = 0.4$. (a) shows the averaged system energy normalized by the self-propulsion velocity as a function of time. Several intermittent spikes in energy is apparent. (b) and (c) show the number of occurrences of each magnitude of energy, i.e. the logarithm of the normalized kinetic energy. In (c) the Gutenberg-Richter law is presented as a solid line. The law is fit using linear regression in the log-log space with a starting point at the highest number of occurrences. 42

4.5 Snapshots of the logarithm of the normalized kinetic energy of particles with $u_0 = 0.4$. The snapshots take place (a) before, (b) during and (c) after an avalanche occurrence. The data is from the same system plotted in Figure 4.4. The bright cluster in (b) can be recognized as largest spike in Figure 4.4a. 44

4.6 Histograms of normalized kinetic energy, Equation (2.41), for periodic systems ranging from $u_0 = 0.1$ to $u_0 = 1.0$. The histograms are generated from the same simulations as Figure 4.2. As the self-propulsion is increased the weight of normalized energies shifts to the right, i.e. to higher energies and the lower bound of the normalized energies increase. For $u_0 = 0.4$ the system starts to flow corresponding to the critical point of the system. Further, the doted line represents the Gutenberg-Richter scaling law (see Figure 4.4c). The slope of the line is -2.58 in the log-N_m space. For the lowest velocities it is likely that the dataset is not sufficiently large to supply representative data of the high magnitudes. 46

4.7 Average normalized kinetic energy as a function of time for different values of the self-propulsion velocity. For $u_0 = 0.4$ the system shows two distinct intermittency events, while for $u_0 = 1.0$ system-wide dynamical arrest is never observed. 47
4.8 Snapshots of the logarithm of the normalized kinetic energy of particles for different values of u_0. The snapshots correspond to the system averaged energy in Figure 4.7. (a) second energy spike from the top plot, (b) highest peak from the middle plot and (c) randomly chosen time from the bottom plot. The number of intermittency events at one point in time increases with the self-propulsion velocity. 49
4.9 Ordering of particles of u_0 at $t = 1607.75$, corresponding to the snapshot in Figure 4.5a. The arrows and the color bar represent the orientation of each particle. The random ordering is observed for all self-propulsion velocities of the system without particle-particle torque. 51
4.10 The time averaged order parameter from Equation 2.34 as a function of self-propulsion velocity u_0. The error bars represent the variance of each point. The large values of the error bars are caused by the transient behaviour of the system. 52
4.11 The time dependent order parameter from Equation 2.34. The different values of u_0 show different behaviour of the system. A globally ordered state is reached for $u_0 = 0.1$ and 0.6, but not for 0.4. 53
4.12 Particle configurations for different times and self-propulsion velocities. The arrows represent the orientation of each particle. The color bar represents the nematic orientation of of each particle, which ranges from $-\pi/2$ to $\pi/2$. The particle extent should in principle be elliptical. The scale of the particles are smaller than their actual size, in order to separate the particles from each other. (a) and (c) show local nematic ordering, while (b) and (d) show a high degree of global nematic ordering. 55
4.13 Histograms of normalized kinetic energy, Equation (2.41), in nematic systems. Selected values of the self-propulsion is plotted. The histograms are generated from the same simulations as Figure 4.12. 56
4.14 Average normalized kinetic energy as a function of time for different values of the self-propulsion velocity in nematic systems. None of the self-propulsion velocities give system-wide dynamical arrest. 57

A.1 Comparison of position between two time steps as a function of time for EM and AB2. The system is simulated for 1000 particles with with no rotational diffusion, i.e. $D_r = 0$. Initially, the particles are distributed homogeneously inside the boundary.The self-propelling velocity of the particles is $u_0 = 10.0$. 72
A.2 Figure (a) shows sampling data of the position for a single particle, and (b) shows the corresponding histogram of the y positions. The boundaries of the well are harmonic with at width of 50. The following parameters has the values, $v_s = 0.5$, $v_0 = 10$, $D_r = 0.001$ and $\Delta t = 0.001$. The simulation is run for 10^8 steps, and the y position is sampled every 1000 step. 74

A.3 Shows different estimations of the sedimentation length of the exponential distribution function. The colored lines represent the following: Blue, the logarithmic values of the histogram in Figure A.2b. Orange, the analytical sedimentation length from Equation A.3. Green, a linear regression of the blue line. Red, the exponential maximum likelihood estimator for the sample data of y. Same simulation parameters as Figure A.2 74

Chapter 1

Introduction

Physics is often thought of as a tool for describing the behaviour of ”dead” objects. The objects themselves do not have a say in how the laws of physics apply to them, such as a rock falling towards the ground due to gravity. Living beings, however, have the possibility to move any direction they like. They are not bound by simple deterministic equations, and can together constitute a collective behaviour. This type of collective motion can be found across all scales of life. Examples of such behaviour are school of fish, epithelial tissue and agarose of bacteria, shown in Figure 1.1. Within soft condensed matter physics there is an increasing effort to classify and understand these collective systems.

”Soft condensed matter is a convenient term for materials in states of matter that are neither simple liquids nor crystalline solids of the type studied in other branches of solid state physics” [5]. A characteristics feature of soft matter is high responsiveness to external forces acting on the system. Soft matter tends to have disordered states with high entropy and large fluctuations. Furthermore, this implies less sharply defined properties in such systems, resulting in a higher degree of material deformation and novel state transitions. In biological matter the characterization of ”soft”-part can be easily understood, as fish or birds does not have a hard defined surface, but have dynamical shapes.

Active matter can be defined as: ”Systems made of a large number of interaction constituents able to convert some source of energy stored in the environment into directed motion” [6]. Many active-matter systems can be identified as soft-matter systems. Similar to soft matter, active matter has a high responsiveness to external changes in the system, and exhibits large fluctuations. In active matter systems the particles often have some sort of anisotropy which might lead to a preferred direction of self-propulsion, converted from the internal energy of the particle. The collective behaviour based on the self-propulsion makes the ordering of orientations an important topic within active matter. Figure 1.1d shows a schematic view of polar and apolar active particles with in polar and nematic ordering. Polar ordering can be observed by the school of fish in Figure 1.1a and nematic ordering by both the tissue and bacteria in Figures 1.1c and 1.1b, respectively.

Some previous studied examples of collective motion in active matter physics are human crowds panicking [7]; groups of animals like, schools of fish [8]; flocks of birds [9];

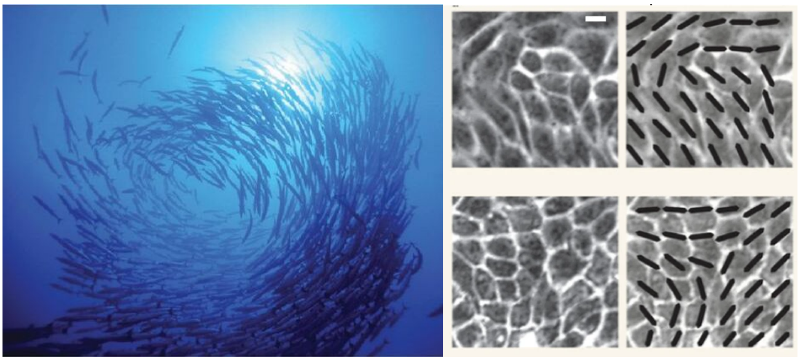

(a) School of fish.

(b) Epithelial tissue.

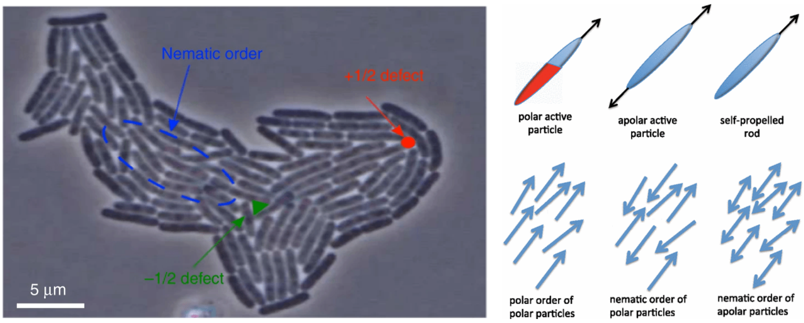
Nematic order
+1/2 defect
−1/2 defect
5 µm
polar active particle
apolar active particle
self-propelled rod
polar order of polar particles
nematic order of polar particles
nematic order of apolar particles

(c) Escherichia coli bacteria.

(d) Polar and apolar particle.

Figure 1.1: Biological active matter. (a) shows a school of fish in circular orientational ordered vortex state (reused from [2]). (b) shows Epithelial tissue of Madine–Darby canine kidney cells (reused from [3]). (c) shows the Escherichia coli bacteria grown on agarose (reused from [3]). (d) shows a illustration of polar and apolar active particles exhibiting polar and nematic order (reused from [4]).

bacteria and self-catalytic colloids [3, 10, 11]; and dynamics of actin filaments [12, 13]. The similarities across these systems suggest set of basic underlying universal features [14]. One of the main goals of the active-matter paradigm is to link these systems to condensed-matter physics. The modeling of active-matter systems can also follow a bottom up approach combining tools from statistical mechanics, soft-matter physics and hydrodynamics [6].

This thesis aims to investigate the explanatory effect of a specific active-matter model. By simulations of this model the goal is to explore various emergent phases and try to understand how phase transitions are governed by the microscopic interactions in the system. In particular, critical dynamics close to transitions will be investigated. The observations will be discussed in order demonstrate connections to well-established physical frameworks. The thesis is a continuation of the master thesis by Andreassen [15] and the project thesis by the author of this work [16].

In this work the focus will be on a periodic boundary system with soft particle-particle interactions. One motivation for using soft repulsion, rather than the hard Lennard-Jones potential, is that living cells have soft boundaries. This thesis is structured as follows. Chapter 2 gives a short introduction to active matter via the Vicsek model and the Langevin equation. Following this, the active matter model, to be used in this thesis, is explained in detail, including boundary conditions and particle-particle interactions. Chapter 3 derives the discrete set of equations from the analytical model and describes the numerical-integration methods used to solve the equations of motion of the active matter system. Chapter 4 presents and discusses the simulations of two active-matter systems, with and without particle-particle alignment, and tries to characterize the emergent phases of the systems. Lastly, Chapter 5 presents the conclusion and suggests further work.

Chapter 2

Theory

In this thesis the term particle will be used to describe all types of constituents in active-matter systems. The term can therefore include bacteria, cells, a schools of fish, a flock of birds or any type of active matter. Regardless, the theory presented in this chapter are applicable to all sorts of active systems.

2.1 The Vicsek model

The Vicsek model, proposed by T. Vicsek et al. [17] in 1995, is perhaps the most influential model in active-matter physics. Despite its simplicity, the model exhibits a phase transition from disordered to ordered global motion. The model is quite simple: It consists of N particles in a square system with length L and periodic boundary conditions. Furthermore, each particle i has a position $\vec{r}_i$ and a velocity $\vec{v}_i$, where the absolute value of the velocity is v. With a discrete time $t_n = n\Delta t$ the position at t_{n+1} will only depend on the previous configuration at t_n. Thus, the equation of motion for each particle is simply

$$\vec{r}_{i,n+1} = \vec{r}_{i,n} + \vec{v}_{i,n}\Delta t = \vec{r}_{i,n} + v\Delta t(\cos\vec{\theta}_{i,n} + \sin\vec{\theta}_{i,n}). \tag{2.1}$$

As seen from the equation it is the angle θ_i that governs the behaviour of the system. This angle is defined as the average orientation of its neighbouring particles (including itself) within a radius r_0 plus a noise term. This is formulated as

$$\theta_{i,n+1} = \langle\theta_{j,n}\rangle_{|\vec{r}_j - \vec{r}_i| < r_0} + \tilde{\eta}, \tag{2.2}$$

where $\tilde{\eta}$ is a stochastic term with uniform distribution in the interval $[-\eta, \eta]$. In this model there are to two competing effects, the energy-like aligning of the particles and the temperature-like randomization of particle orientations.

For certain limits this model takes on the form of other familiar models. In the limit $v \to 0$ the Vicsek model is reduced to the well-known XY-model as the particles will become spatially fixed (the XY-model is presented in Section 2.5.5). If the velocity reaches the limit $v \to \infty$, the particles will effectively mix up all its neighbouring particles between each time step. This corresponds to a mean-field spin model for ferromagnets.

In the Vicsek model the net momentum is not conserved during ”collisions” of particles due to the enforcement of constant particle velocity. The sum of the velocities therefore constitutes a meaningful order parameter, defined as

$$\Pi \equiv \frac{1}{Nv} |\sum_i \vec{v}_i|. \tag{2.3}$$

The paper [17] written by Vicsek et. al. presents a clear dependence between the order parameter Π and the magnitude η of the stochastic noise term. With zero noise, which implies a temperature of zero degrees, the order parameter becomes unity, i.e. a fully ordered system. At the limit of infinite temperature, given by $\eta = \pi$, the order parameter becomes zero. In this limit the alignment contributions from neighbours are negligible compared to the stochastic noise and it follows that the orientations of particles are totally random. In the regime around $\eta \approx 0.3\pi$ the results show a transition from a ordered to a disordered state. A more recent study demonstrates that in this regime the state can be a mix between disordered and ordered phases [18].

2.2 Langevin equation

The Langevin equation is a stochastic differential equation describing the time evolution of a system based on degrees of freedom. The equation describes a type of Brownian motion, namely the random movements of a particle in a fluid due to collisions in the fluid. The original Langevin equation [19] is formulated as

$$m\frac{d^2\vec{r}}{dt^2} = -\gamma\frac{d\vec{r}}{dt} + \vec{\xi}(t). \tag{2.4}$$

The degree of freedom of this system is the position $\vec{r}$ of the particle. Furthermore, m denotes the mass of the particle, γ describes the magnitude of the sum of viscous forces proportional to the particle’s velocity given from Stokes’ law [20] and $\vec{\xi}(t)$ is a noise term which represents the random collisions of the particle with the surrounding fluid. The force $\vec{\xi}(t)$ has a Gaussian probability distribution.

2.3 Active Brownian dynamics

A system of active Brownian particles is different from a system of particles following the Langevin equation due to the fact that these particles have a self-propulsion force F_a. This force will give the particles a constant self-propulsion velocity v_0 parallel to each particle’s orientation θ. Keeping the self-propulsion velocity aligned with the particle orientation will mimic the typical hydrodynamic forces caused by particles moving in confined systems [21]. The self-propulsion forces originate form the particles themselves, and not from any external potentials in the systems. This means that the self-propulsion forces exert a net force on the system, making this a non-equilibrium system. With the use of Equation (2.4), the equation of motion for active Brownian particles takes on the following form

$$m\frac{d^2\vec{r}}{dt^2} = -\gamma\frac{d\vec{r}}{dt} + \vec{\xi}(t) + F_a\vec{u(t)}. \tag{2.5}$$

Here $\vec{u}(t)$ is the direction of the self-propulsion force. The direction θ of the particle will also follow the Langevin equation, given in Equation (2.4) [6].

The self-propulsion velocity of active particles gives rise to considerable viscous drag forces. These forces cannot be neglected as they ensure that the particles does not accelerate without bounds. Assuming a very low Reynolds number (which holds for the motion of bacteria and other micro-swimmers [22][23]) makes the viscous drag forces essentially cancel out all the other forces. This gives rise to an important limiting case of Equation (2.5) called overdamped Brownian motion. By setting the left hand side of Equation (2.5) to zero, and omitting the noise term, an active Brownian particle can be described by the equations

$$\frac{d\vec{r}(t)}{dt} = v_0\vec{u}(t), \tag{2.6}$$

$$\frac{d\theta(t)}{dt} = \sqrt{2D_r}\eta(t), \tag{2.7}$$

$$\vec{u}(t) = \cos\theta(t)\hat{x} + \sin\theta(t)\hat{y}. \tag{2.8}$$

Usually, in Brownian dynamics there is a stochastic noise term with a random direction and amplitude at each time t. However, in Equation (2.6) this term is omitted as the diffusive motion of the particle is dominated by self-propulsion swimming. This self-propulsion velocity is not affected by a noise term in the position of the particle. As seen for Equation (2.7), the diffusion in the system is achieved by letting the direction θ obey the massless Langevin equitation. The of direction θ of each particle follows an individual one dimensional random walk. This set of equations resembles of Gaussian random walk.

The self-propulsion force F_a has been replaced by the self-propulsion velocity $v_0 = F_a/\gamma_t$, with γ_t as the translation friction coefficient. In this overdamped regime, physical quantity m has dropped out, making this a non-inertial system. The friction coefficient γ has dropped out of the equations, but will reappear later as boundary forces and particle-particle forces are introduced.

The term $\eta(t)$ is a stochastic process representing rotation of the particle orientation due to collision with the surrounding fluid. The magnitude of the fluctuations in the orientation is equal to $\sqrt{2D_r}$, where D_r is the rotational diffusion coefficient. The term $\eta(t)$ follows a uniform probability distribution with the properties

$$\langle\eta(t)\rangle = 0, \tag{2.9}$$

$$\langle\eta(t_1)\eta(t_2)\rangle = \delta(t_2 - t_1). \tag{2.10}$$

A uniform probability distribution is used instead of a Gaussian probability distribution mainly because the former requires notably less computational power to estimate. As long as the the central limit theorem holds for the chosen distribution, the macroscopic behaviour of the system should be the same. The most important factors are that the probability distribution is symmetric, Equation (2.9) and that the correlation function is correct, Equation (2.10).

The definition of the rotational diffusion coefficient D_r ensures that the characteristic decorrelation time of the particle orientation is $\tau_0 = 1/D_r$ [24]. From the decorrelation time one can define the persistent length

$$l_p = v_0 \tau_0 = \frac{v_0}{D_r}. \tag{2.11}$$

This length is a typical value for how far a particle can maintain linear movement before changing direction. The decorrelation time τ_0 is therefore a temporal measure of how long a particle can maintain its direction before the stochastic nature of the system will randomize its path. As the rotational diffusion coefficient $D_r \to 0$, and thus the persistent length $l_p \to \infty$, the stochastic nature of the system vanishes. Oppositely, as the rotational diffusion coefficient becomes very large, i.e. $D_r \to \infty$, the persistent length become very small, i.e. $l_p \to 0$. The system is now dominated by the stochastic term, and other effects related to the orientation of the particle will be negligible.

The self-propulsion force and velocity originates from consummation of potential energy in the particle, which is transferred into the system as mechanical energy [25]. This mechanical energy is again dissipated in the surrounding system of the active particle as thermal energy thorough the viscous drag forces on the left hand side of Equation (2.6). This means that as long as the active particles maintain their self propelling velocity the system will gradually increase its thermal energy.

2.3.1 Expectation values of free active Brownian particles

As the equations of motion for free active Brownian particles consist of ordinary differential equations, the orientation of the particle can be found. Equation (2.7) can be solved analytically with Itô calculus to find the orientation of the particle as a function of time

$$\theta(t) = \int_0^t dt' \sqrt{2D_r}\eta(t'), \tag{2.12}$$

with $\theta(0) = 0$. Furthermore, the first property of the distribution function from Equation (2.9) implies that the expected value of the orientation is

$$\langle \theta(t) \rangle = \int_0^t dt' \sqrt{2D_r}\langle \eta(t') \rangle = 0. \tag{2.13}$$

The second property of the distribution function, as shown in Equation (2.10), gives the average angle squared as

$$\langle [\theta(t)]^2 \rangle = \int_0^t dt' \int_0^t dt'' 2D_r \langle \eta(t')\eta(t'') \rangle = 2D_r t. \tag{2.14}$$

This shows that the absolute value of the orientation $\theta(t)$ should be proportional with the square root of the time t.

Another interesting quantity that can be found for free active Brownian motion is the the directionality of the self-propulsion velocity. The directionality is the ability of the particle to keep its orientation constant during a typical persistence time $\tau = D_r^{-1}$ [6]. The directionality is described by

$$\langle \vec{u}(t) \cdot \vec{u}(0) \rangle = v_0^2 \mathrm{e}^{-t/\tau}. \tag{2.15}$$

The physical interpretation of the analytical values for the motion of the particle in this section is interesting as they show that the free active particles will have a diffusive behaviour. These values will also be important in developing of numerical simulation tool to ensure whether the diffusive behaviour of the tool is correct.

2.4 System boundary conditions

Like any physical system, a system of active Brownian particles will have a boundary. Such a boundary may for instance act as a hard wall (step potential) and scatter colliding particles or a soft wall gradually reorienting the particles. The boundaries may also exert a torque on a particle located in close proximity. Depending on the type of particle and boundary this torque may either try to orientate the particles normal to or parallel to the boundary [26].

Representing physical boundaries mathematically may be challenging, particularly when used in numerical models. For hard walls the abrupt changes in particle restraints creates issues with the stability of numerical integration schemes. To make rigorous mathematical models and to reduce numerical integration issues, continuous potentials can be utilized to model the system boundaries.

A general boundary potential $V_\mathrm{b}(\vec{r})$ acting on a particle will give rise to a force $\vec{F}_\mathrm{b}(\vec{r})$ and, if the particle has a non-circular extent, a torque $\Gamma_\mathrm{b}(\vec{r})$ as well. An illustration of boundary force and torque is depicted in Figure 2.1. The force will push/pull the particles away from/towards the wall, while the torque will rotate the direction of the particles. The force from a general position-dependent potential is defined by

$$\vec{F}_\mathrm{b}(\vec{r}) = -\nabla V_\mathrm{b}(\vec{r}). \tag{2.16}$$

The torque from a force on a elliptical particle is derived in the supplementary information of the paper by Solon et. al. [27]. In summary a particle with the form of an ellipse, with uniform density and major and minor semi-axes of length a and b respectively, the torque applied by a force $\vec{F}(\vec{r})$ on an area element of the ellipse is

$$\vec{\gamma} = \vec{r_p} \times \vec{F}_\mathrm{b}(\vec{r}). \tag{2.17}$$

Here the distance r_p is from the centre of the particle to a point on the edge or inside the ellipse. The total torque is then defined as the integral of all area elements of the ellipse with a corresponding torque element γ,

$$\Gamma_\mathrm{b} = \frac{m}{\pi ab} \int dx_p dy_p \gamma, \tag{2.18}$$

where the integral is of the major and minor semi-axis x_p and y_p, respectively, of the elliptical particle. In the equation m is the mass of the particle.

The force and torque arising from the boundary potential $V_{\mathrm{b}}(\vec{r})$ will each add one term to Equations (2.6) and (2.7) in the following way,

$$\frac{d\vec{r}(t)}{dt} = v_0\vec{u}(t) + \vec{F}_{\mathrm{b}}(\vec{r})/\gamma_t, \tag{2.19}$$

$$\frac{d\theta(t)}{dt} = \sqrt{2D_r}\eta(t) + \Gamma_{\mathrm{b}}(\vec{r},\theta)/\gamma_r, \tag{2.20}$$

where γ_t and γ_r are the translational and rotational friction coefficients, respectively. From this it is clear that close to the system boundary the particle velocity will not necessarily have the constant value v_0 and the direction of the particle will rotate towards parallel alignment with the boundary.

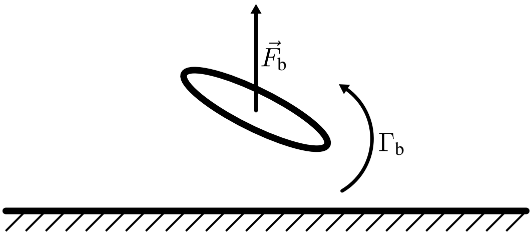

Figure 2.1: Illustration of a particle interacting with a boundary. The force is denoted as $\vec{F}_{\mathrm{b}}$ and the torque as Γ_{b}, as in Equations (2.19) and (2.20), respectively.

2.4.1 Periodic boundary conditions

For some systems, the effect of the boundary is of no interest, and periodic boundary conditions are used. This type of boundary is often used to approximating large (infinite) systems. The periodic boundary is realized by defining a unit cell in which the edges in each direction are connected. To visualize this, a rectangular system in the xy-plan can be used as a unit cell. First the edges of the rectangle along the x-direction is connected by ”rolling” the rectangle into a cylinder, stretching along the x-axis. Afterwards, the two ends of the cylinder are connected by bending the cylinder around the y-axis. The final system takes on the shape of a torus. The surface of a torus does not have any boundaries, and, as seen, is easily transposable into a rectangle.

For an active systems of length L and height H centered around the origin, the periodic boundary condition can be imposed by a set of spatial conditions,

$$x = \begin{cases} x - L, & \text{if } x > L/2, \\ x + L, & \text{if } x < -L/2, \\ x, & \text{else.} \end{cases} \qquad y = \begin{cases} y - H, & \text{if } y > H/2, \\ y + H, & \text{if } y < -H/2, \\ y, & \text{else,} \end{cases} \tag{2.21}$$

The angle θ of each particle is kept constant although the x- and/or y- values are changed.

Periodic boundary conditions are a powerful tool to simulate approximated infinite systems based on a unit cell of any size. The properties of large systems can categorized without exhausting all available computational resources. However, if the unit cell is too small, unwanted effects may occur. For instance, a particle may interact with itself across the periodic boarder, which can lead to a behaviour that is not physically justifiable.

For active systems, periodic boundary conditions often allows the particles to maintain a higher average velocity, as there are no boundaries to stop the self-propulsion velocity of the particles. However, most observable active systems are limited within a set of boundaries, which motivates the use of fixed size boundaries. The number of active particles within a fixed boundary can vary. For systems with a high number particles, the computational effort becomes too high to handle. Most existing simulations contain around 1000 particles and some up to 10000 [27, 28, 29, 30, 31]. For physical systems with a number of particles higher than this, periodic boundary conditions may be beneficial.

2.5 Particle-particle interaction

In the Vicsek model the particles have a point-like behaviour. By introducing forces acting between neighbouring particles each particle will occupy a certain space and therefore also acquire an implicit particle size. As with the boundary conditions, the forces interacting between particles in active Brownian systems can be described using potentials. The type of interaction can vary in range and strength depending on how the potential is defined.

A particle can have a well defined direction based on a non-circular shape or implicit internal direction [32]. The direction of a particle can be directly or indirectly dependent on the particles in the rest of the system. An indirect dependency can be found by a particle wanting its internal direction to be aligned with the movement of the particle itself [28]. The movement of the particle itself is of course dependent on the movement of the rest of the particles in the system. In this situation there is no direct interaction between the directions of the particles in the system.

The change of direction of a particle can also be explicitly dependent on the directions of its neighbouring particles, where the interactions can be described with torques [18]. In order for a particle to experience an external torque, the shape of the particle must be non-circular, typically modeled as an ellipse, or have a non-geometrical asymmetry, such as a polarity or magnetic moment. A torque related to the shape of a particle, will typically result in alignment of the particles. The alignment could be parallel, which is known as polar ordering or a combination between parallel and antiparallel, which is known as nematic ordering. An illustration of the two ordering types can be seen in Figure 1.1d. This thesis will focus on short range interactions and explicit defined nematic alignment, where the forces and torques acting on each particle will only depend on neighbouring particles within a couple of particle radii.

For a general Brownian system the particle-particle interaction consists of the force $\vec{F}_{\text{pp}}(\vec{r}_{ij})$ and the torque $\Gamma_{\text{pp}}(\vec{r}_{ij})$, acting on particle i from particle j. An illustration of particle-particle force and torque is depicted in Figure 2.2. By adding these particle-particle interactions to Equations (2.19) and (2.20), the final equations of motion for the system becomes,

$$\frac{d\vec{r}_i(t)}{dt} = v_0\vec{u}_i(t) + \big(\vec{F}_{\text{b}}(\vec{r}_i) + \sum_{j\neq i}\vec{F}_{\text{pp}}(\vec{r}_{ij})\big)/\gamma_t, \tag{2.22}$$

$$\frac{d\theta_i(t)}{dt} = \sqrt{2D_r}\eta(t) + \big(\Gamma_{\text{b}}(\vec{r}_i) + \sum_{j\neq i}\Gamma_{\text{pp}}(\vec{r}_{ij})\big)/\gamma_r. \tag{2.23}$$

In these equations $\vec{r}_i$ is the position of particle i and $\vec{r}_{ij} = \vec{r}_i - \vec{r}_j$ is the distance between particle i and j. The sums are in principle of all N particles making up the system. However, since the focus in this thesis is short range interactions, the sum will only be made up of the neighbours within a certain radius of each particle. Note that the distance $\vec{r}_{ij}$ must be carefully considered in systems with periodic boundaries. Here the smallest value of $\vec{r}_{ij}$ should be used, if this distance is calculated across all periodic boarders.

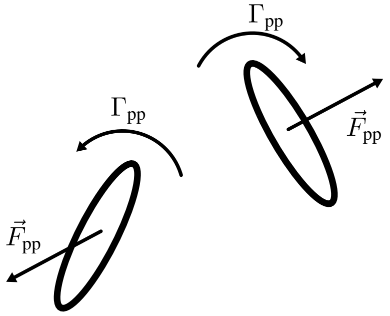

Figure 2.2: Illustration of particle-particle interaction for two particles. The inter-particle forces are denoted as $\vec{F}_{\text{pp}}$ and torques as Γ_{pp}, as in Equations (2.22) and (2.23), respectively.

2.5.1 Weeks-Chandler-Andersen potential

A hard sphere potential, often used in molecular dynamics to describe particle-particle interaction, is the Weeks-Chandler-Andersen (WCA) potential [33]. It is defined as,

$$V_{\text{WCA}}(r_{ij}) = \begin{cases} 4((\frac{\sigma}{r_{ij}})^{12} - (\frac{\sigma}{r_{ij}})^6) + 1, & \text{if } r_{ij} \leq 2^{1/6}\sigma, \\ 0, & \text{else.} \end{cases} \tag{2.24}$$

where σ defines the range of the potential, and r_{ij} is the distance between particle i and j.

As seen from Equation (2.24), the WCA potential presented here is the Lennard-Jones potential [34] truncated at its minimum value $r = 2^{1/6}\sigma$, the depth of the potential set to 1, and shifted upwards by 1 such that the potential is zero at the cutoff distance. The WCA potential and the Lennard-Jones potential are commonly used for active matter simulations [30].

2.5.2 Harmonic interaction potential

The hard WCA potential is typically used to simulate molecular interactions and may not be suitable to describe all types of systems. This type of hard sphere potential is typically used for smaller particles such as molecules in fluids [35]. For systems consisting of larger particles, such as cells or bacteria other potentials may be more suitable. One of these is the harmonic potential [31, 28] defined as,

$$V_{\mathrm{H}}(r_{ij}) = \begin{cases} \frac{\lambda}{2}(r_{ij} - r_{\mathrm{c}})^2, & \text{if } r_{ij} \leq r_{\mathrm{c}}, \\ 0, & \text{else.} \end{cases} \tag{2.25}$$

Here, r_{ij} is the distance between particle i and j, r_{c} is the cutoff distance of the potential, and λ is the strength of the potential. Using Equation (2.16) the force becomes,

$$\vec{F}_{\mathrm{H}}(\vec{r}_{ij}) = \begin{cases} -\lambda(r_{ij} - r_c)\hat{r}_{ij}, & \text{if } |\vec{r}_{ij}| \leq r_{\mathrm{c}}, \\ 0, & \text{else,} \end{cases} \tag{2.26}$$

where $\hat{r}_{ij}$ is the direction of the vector $\vec{r}_{ij}$.

The expression shows a linear force, quite different from the force the WCA potential produces. Two possible interpretations of the soft potential made by author will follow.

This type of soft potential can be physically interpreted as a particle with a compressible surface. When two particles collide their velocity will be reduced as the particles are compressed together. If the two particles move directly towards each other, the particles will reach a point where the particles are fully compressed with zero velocity, and the particles will stay arrested.

The other interpretation is that each particle has a hard surface, but can ”sense” its surroundings. The idea is that an active particle will turn away from a neighbouring particle before a direct collision occurs. A soft potential can imitate this behaviour, by gradually changing the orientation of the particle. The change occurs when the two particle are within a certain distance of each other, but before the hard surfaces collide.

From the linearly scaling force in Equation 2.26 and by assuming an elliptical shaped particle with major and minor semi-axis as a and b respectively, the torque on a nematic particle from a neighbouring particle can be derived as,

$$\Gamma(\vec{r}_{ij}, \theta_i, \theta_j) = \begin{cases} \lambda\kappa \sin\big(2(\theta_i - \theta_j)\big), & \text{if } |\vec{r}_{ij}| \leq r_{\mathrm{c}}, \\ 0, & \text{else.} \end{cases} \tag{2.27}$$

with $\kappa = \frac{m}{8}(a^2 - b^2)$, where the mass m is set to 1. θ_i and θ_j are the directions of particles i and j. The product $\lambda\kappa$ is the coupling strength of the torque acting on the particle. The factor 2 is due to the assumed nematic nature of the particles. This ensures that the parallel and antiparallel alignment of the particles generate zero torque.

For the derivation of the force it is assumed that the whole particle is assumed either inside or outside the the cutoff radius r_c at one point in time. The simple and neat expression for the torque is specific to the harmonic potential (the derivation can be found in [27]). Expressions for other potentials will in general be much more complicated.

2.5.3 Particle radius

In the Vicsek model a point-like particle approached is used. The interaction between neighbouring particles, described by Equation (2.2), is limited by the interaction length r_0. This length can therefore be interpreted as the diameter of the particle. However, with this interpretation the physical extent of point-like particle, two neighbouring particle may partially or fully overlap. This can be an issue as the model should represent actual physical quantities.

By introducing inter-particle forces, a more well defined, yet not completely sound, description of the particles' physical extent can be defined. Again, as in the Vicsek model, the interaction cutoff radius, but now for the forces acting on the particle, can be used as the particle diameter. This gives a good measure of the particle size for hard potentials such as the WCA potential, but for softer potentials such as the harmonic potential the measure is not as accurate. For two particles interacting with the harmonic potential, the particles can move quite far ”into” each others potentials before the accompanying forces will be large enough to stop the particles.

A second method can be used for defining the particle size, following the discussion of soft potentials in the previous paragraph. The idea is that the particle radius can be calculated based on the length of which two particles can penetrate each others potentials. Mathematically this can be derived from Equation (2.22), which yields,

$$-\nabla V_{pp}(2r_a) = v_0, \tag{2.28}$$

where $2r_a$ is inter-particle distance from the centre of each particle, which implies that r_a is the particle radius. With this interpretation the particle radius is directly dependent on self-propulsion velocity. In this respect, for simulation purposes where the velocity if varied, one could define a reference velocity and calculate the particle radius with respect to this.

The situation can be interpreted in the following way: Two active particles with a constant swim velocity will travel towards each other. At some point they will enter each others potentials. As they move further into each others potentials, the repulsive force acting on each particle will become larger until the repulsive force will balance the self-propulsion force of each particle, and the particles will reach full arrest. At this point, the inter-particle distance can be used to define the particle radius.

2.5.4 Packing fraction

As seen from the discussion above, there is no particular good way to defined the size of particles that are only described by their interaction potential and torque. As a consequence, the density of such a system is also troublesome to defined. In order to have a reference of the density of the system, the packing fraction of the system can be used. In order to calculate the packing fraction, a particle radius is needed, which for instance can be calculated by Equation (2.28) together with a reference velocity. For a two-dimensional system the area packing fraction is simply defined as,

$$\rho = \frac{N\pi r_a^2}{A_\mathrm{s}}, \tag{2.29}$$

where N is the number of particles and A_s is the area of the system.

For an active system using the the harmonic potential for particle-particle interaction, the packing fraction can become larger than 1. As a comparison, the random packing fraction of non-interacting hard spheres of uniform diameter is calculated to be 0.82 [36]. This is the highest area fraction one would expect to occur for random placed particles. This should be compared with the fraction in hexagonal close packing, 0.907, and in cubical close packing, 0.785 in two dimensions.

With the harmonic potential in Equation (2.25) and a packing fraction higher than 1, the particles in the system will always interact with its neighbouring particles. Which means the particles will always be subject to force and an associated energy (see Section 2.9 for further discussions). If the packing fraction becomes very large, the particles may be subject to extreme forces leading to non-physically velocities of the particle. This is merely a weakness of the model, and is not of physical meaning. In reality the particles would probably experience irreversible deformation before reaching such a high packing fractions.

In the equation of motion, Equation (2.22), the right hand side is normally the viscous drag forces from the medium of the colloidal suspension. In extreme dense systems the colloidal suspension will consist almost completely of active particles and no medium of suspension for the drag forces to act on. This raises the question of the origin of the viscous forces in such a system. One could argue that the drag forces is a result of neighbouring active particles. This argument is only valid for a systems with random orientations of the particles. However, in highly ordered systems, all the particles travel in the same directions, and shear forces for neighbouring particles will disappear as the particles are traveling in the same direction. In dense two-dimensional system the drag forces could be caused by the confinement (in the third direction) of the particles, which would be present regardless of the ordering of the system.

Alternatively, Equation (2.22) can be interpreted in a different manner. For this interpretation the active particles are assumed to move with a constant velocity, not necessarily equal to the self-propulsion velocity, until a force acts on the particle. This can be written as $\Delta v_i(t) = F_i(\vec{r_i})/\gamma_t$. This is a loosely rewritten version of Equation (2.22), and is not mathematically correct, but only used as an aid in the interpretation of an extremely dense system. The equation implies that the velocity of a particle is only dependent on its neighbouring particles (or boundary). The issue of the origin of the viscous drag forces is omitted by stating that the self-propulsion velocity and viscous drag forces sum up to zero. For a free active particle, this implies that the particle will maintain a constant velocity.

2.5.5 Alignment torque with the XY-model

A purely geometric example of alignment caused by torque is seen in Equation (2.27). However, the alignment of particles is a field that is widely studied within statistical mechanics, with different origins.

Classical XY-model

Examples of particle-particle alignment are for instance the Ising model, the Heisenberg model, and of interest in this study, the classical XY-model. The latter describes the energy configuration of a lattice system, where each lattice site i has a directional unit-length vector given by $\vec{s_j} = (\cos(\theta_i), \sin(\theta_i))$ representing a spin configuration. With a translation-invariant interaction $J_{ij} = J(i-j)$ and a spatially dependent external field $\vec{h}_j = (h_j, 0)$, the energy of the spin configuration can be written as

$$H(\vec{s}) = -\sum_{i \neq j} J_{ij} \vec{s}_i \vec{s}_j - \sum_j \vec{h}_j \vec{s}_j = -\sum_{i \neq j} J_{ij} \cos(\theta_i - \theta_j) - \sum_j h_j \cos(\theta_j). \quad (2.30)$$

For no external field, the energy of the spin configuration will have its minimal value when all the particles are aligned. In other words θ_i should equal θ_j for all values of i and j. The actually orientation of the system does not affect the energy, as long as all the particles are aligned. This is an example of a polar ordered system.

Flying XY-model

The Vicsek model uses a simple average of neighbouring particles to alter the orientations in the system. When particle-particle interactions are included in the active-matter model, the particles obtain a physical extent and it is therefore more natural to model the change of orientations by using particle-particle alignment torques.

A simple way to do this, is to modify the classical XY-model to active-matter systems. The interactions between the particles will follow the same principles, but the particles will no longer be restricted to lattice sites. This type of alignment is referred to as the flying XY-model in the paper by Farrell et. al. [29] and also used in the simulations by Solon et. al. [27]. The torque for the flying XY-model can be defined as,

$$\Gamma(\theta_i, \theta_j, r_i) = \begin{cases} \frac{\gamma}{\mathcal{N}(r_i)} \sin(\theta_j - \theta_i), & r \leq r_\mathrm{c}, \\ 0, & r > r_\mathrm{c}. \end{cases} \quad (2.31)$$

Here r_i is position of particle i, and the radius r_c is the range in which a particle will interact with neighbouring particles. The coupling strength of the alignment torque is given by γ and $\mathcal{N}(r_i)$ is the number of neighbours defined as,

$$\mathcal{N}(r_i) = \sum_{r_{ij} \leq r_\mathrm{c}} H(r_\mathrm{c} - r_{ij}). \quad (2.32)$$

The sum is of all neighbouring particles within the cutoff radius, r_{ij} is the distance between partile i and j and $H(r)$ is the Heaviside step function.

For no external field ($\vec{h}_j = 0$) the flying XY-model shows great resemblance to the XY-model, where the main differences is that the flying XY-model interacts with neighbours within a certain radius, while the classical XY-model interacts with certain neighbouring lattice points.

The flying XY-model is defined for polar particles. In order to adapt the model to nematic particles, parallel and antiparallel ordering must be equitable. To achieve this a factor 2 must be multiplied with the argument in the sine function in Equation (2.31). This yields the following equation,

$$\Gamma(\theta_i, \theta_j, r) = \begin{cases} \frac{\gamma}{\mathcal{N}(r)} \sin\left(2(\theta_j - \theta_i)\right), & r \leq r_{\mathrm{c}}, \\ 0, & r > r_{\mathrm{c}}. \end{cases} \tag{2.33}$$

This equation is almost identical to Equation (2.27), the geometrically derived torque for the harmonic potential. The main difference is the term $\mathcal{N}(r)$, which simply is another ways of writing the average of all torques acting on a single particle. The coupling strength γ is equivalent with the product of the factors $\lambda\kappa$ in Equation (2.27). This implies that the information about the shape of the particle in contained withing the factor γ. This nematic version of the flying XY-model will be used in this thesis.

2.6 Collective motion in confinement

As with the Vicsek model, a general active Brownian systems can become ordered. Similar to Equation (2.3), an order parameter can be defined to measure the degree of ordering. For high density systems the particles often have very slow or no movement at all. Therefore the order parameter should not be based on the particles velocities, but rather the orientation of the particle. For a two dimensional nematic active matter system the order parameter can be defined as [37],

$$\Pi_{\upharpoonleft\downharpoonright}(t) = 2\langle\cos^2\phi_i(t)\rangle - 1. \tag{2.34}$$

Here ϕ_i is the angle between the orientation vector of particle i and the nematic director. The nematic director is the mean orientation of the particles. The average $\langle\ldots\rangle$ is of all the particle at the time t. The square of the cosine ensures that parallel and antiparallel ordering is equitable. The order parameter ranges from -1 to 1, where -1 is a ordered state normal to the nematic director, 0 is a fully disordered state and 1 is a fully ordered state. The ratio of parallel and and antiparallel ordering is not measured.

When calculating the nematic director, special care must be taken, as two particles with antiparallel directions should contribute to the same angle in the system average. An orientation average over a perfect antiparallel ordered system, would yield a director normal to the orientation of all the particles. To overcome this issue all orientations can be shifted to the first and fourth quadrant, i.e. $\theta \in \langle -\pi/2, \pi/2]$ and then averaged.

As an active-matter system is under constant fluctuations due to its stochastic nature, the time average of the order parameter might also be of interest,

$$\langle\Pi_{\upharpoonleft\downharpoonright}\rangle_t = \frac{1}{N}\sum_{n=1}^{N}\Pi_{\upharpoonleft\downharpoonright}(t_n). \tag{2.35}$$

Here, the sampling of ordering is assumed discretized, and t_n is the discretized time.

For an unstable system or a system with a long transient, the temporal average of the order parameter may be misleading when it comes to the state of the system. The ordering of the system might vary quite much with time, especially around critical phases. Therefore, the standard deviation of the order parameter is an important value. The time dependent standard deviation is defined as

$$\Delta\Pi_{\uparrow\downarrow} = \sqrt{\frac{1}{N-1}\sum_{n=1}^{N}(\Pi_{\uparrow\downarrow}(t_n) - \langle\Pi_{\uparrow\downarrow}\rangle_t)^2}. \tag{2.36}$$

As with the average order parameter, the equation for the fluctuations is derived based on a discrete set of data for the ordering of the system.

$\Delta\Pi_{\uparrow\downarrow}$ can now be interpreted as a quantitative measure of the fluctuations in the system. These fluctuations are a measure of the contributions to the disordering of the system made by random noise, compared to particle-particle interactions ordering the system. A high measure of fluctuations indicates an unstable state, while a low measure of fluctuations indicates a stable state.

2.7 Spontaneous symmetry breaking

Spontaneous symmetry breaking is the phenomenon where a physical system in a symmetric state ends up in an asymmetric state [38]. In particular it can describe systems where the lowest energy in the system does not exhibit the same symmetry as other states. The symmetry is often related to an order parameter, the quantity which breaks the symmetry under consideration. Since the order parameter in Equation (2.34) is not translational and rotational invariant for all transformations, spontaneous symmetry breaking may arise.

An example of spontaneous symmetry breaking for condensed matter physics is ferromagnetism which breaks the continuous symmetry of magnetic moments of the ferromagnet below the critical temperature, i.e. the Curie temperature, and without any external field defining the direction. Above the critical temperature, the ferromagnet consists of local oriented magnetic domains, such that the net magnetization of the ferromagnet is zero. Below the critical temperature the magnetic moments of the ferromagnet become aligned with their neighbours, and spontaneous symmetry breaking has occurred.

According to the Mermin and Wagner theorem [39], long-range ordering at finite temperatures cannot occur in one- and two-dimensional equilibrium systems with short range interactions. This means that spontaneous magnetization below the Curie temperature only occurs in a three-dimensional system.

From Section 2.6 the nematic ordering of active-matter systems can be interpreted as an analogy to magnetic ordering in ferromagnetic systems. The order parameter in ferromagnetic system is the magnetic moments while in the active matter system it is the orientation of the particles. In the same way that a ferromagnetic system experiences spontaneous symmetry breaking when the magnetic moments align under the critical temperature, the active-matter system will break symmetry if the orientation of the particles order below a certain value of the rotational diffusion coefficient D_r.

From previous studies it has been shown that active-matter systems can have spontaneous symmetry breaking, even in two dimensions [40, 41]. The equations of motion of a periodically bound, interacting active particle system, as described in this chapter, do not have a preferred orientation of the particle. The orientation of each particle is however based on the torque and stochastic noise acting on it. Below a certain limit of the rotational diffusion coefficient the system will experience irreversibly transition to an ordered state, which implies that spontaneous symmetry breaking has occurred. The apparent symmetry in the system expressed by the equations of motion will in this case no longer be present.

2.8 Four-point susceptibility function

The four-point susceptibility function is a measure of how much a particle correlation function fluctuates around its average value. The function can be used to characterize spatio-temporal heterogeneous dynamics. The four-point susceptibility function is often used in granular material physics to categorize dynamical heterogeneity close to the liquid-glass transition [42, 43, 44], but can also be utilized on active matter systems. The function can be calculated both from purely numerical simulations and experimental results. The expression of the four-point susceptibility function is defined as the variance of the particle correlation function, a order parameter of the system [45], in the following way,

$$\chi_4(\tau) \equiv N[\langle Q_t^2(\tau)\rangle - \langle Q_t(\tau)\rangle^2]. \tag{2.37}$$

The order parameter is denoted by $Q_t(\tau)$, where τ is a time interval. High values of $\chi_4(\tau)$ is caused by large fluctuations in the order parameter and therefore indicates significant spatial heterogeneous dynamics in the system.

The order parameter measures the movement of particles, constructed in such a way that the contribution form each particle decays from 1 to 0 as the time increases from t to $t + \tau$ and the particle moves some related distance. The order parameter can be defined in different ways. One such correlation function is the intermediate scattering function, the Fourier transform of the Van Hove function [46, 47]. Another, is the self-overlap function, which will be used in this thesis.

Toninelli et al. [1] have used mode coupling theory to characterize the behaviour of χ_4 near the critical temperature for the glass transition. Mode coupling theory will not be discussed in this thesis. The main result of the study can be summarized by the four-point susceptibility and its assigned time sectors shown in Figure 2.3.

In the figure each time sector spans a time interval with a distinct type of dynamics. Each type of dynamic is identified by a gradient μ in the log-log space, i.e. a power law t^μ, as seen in Figure 2.3. From left to right the regimes are the following, ballistic, elastic, early beta, plateau, late beta and alpha regime. The ballistic regime is valid for very short time intervals, and each individual particle behaves as a free-particle. For particles exhibiting Brownian motion, the sector denoted as the ballistic regime becomes a diffusive regime with $\mu = 2$ instead of 4. In the consecutive time sector, the elastic regime, the particles start to collide, where the kinetic energy is preserved in the collisions.

Following the elastic regime, the beta regime starts. The beta regime consists of an early and a late sector along with a plateau. In general β-relaxation consists of local motion of particles and is the precursor to α-relaxation [48]. In the beta regime the collective phenomenon of the system sets in. As the time interval further increase the alpha regime is reached where the four-point correlation function has a peak, before it at last decays to zero. This sector is exhibits α-relaxation, where the system is collectively relaxed in means of cooperative particle motion: When one particle moves another particle moves by closely following the first particle [49]. As the temperature is lowered the elastic regime is expected to extend up to the alpha regime, and all the intermediate regimes will disappear.

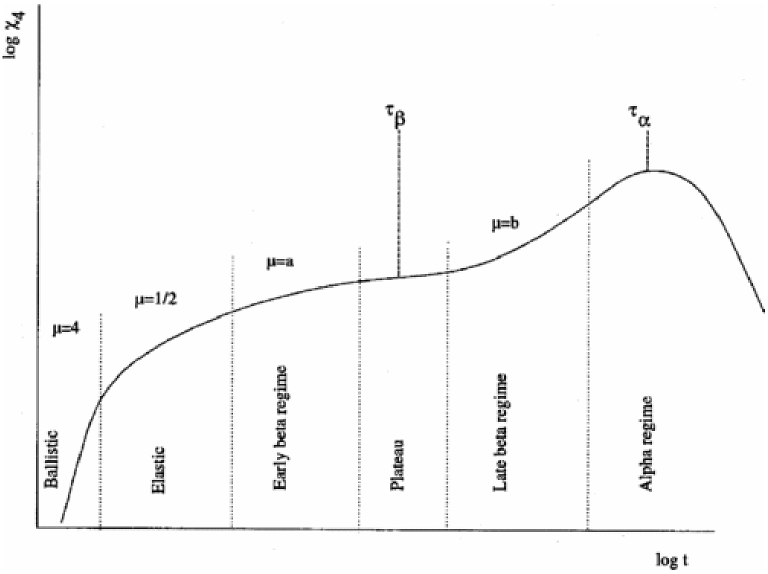

Figure 2.3: Sketch of the time behavior $\chi_4(t)$, for different time regimes, derived from from mode coupling theory close to the glass transition temperature. Figure reused from [1].

As mention above, Figure 2.3 is primarily defined close to the glass transition temperature. However, in active systems the effect of the temperature is usually negligible compared to the self-propulsion velocity of the particle. The presented behaviour of four-point susceptibility function can still be of great use, if the temperature dependence of the system is substituted with self-propulsion velocity dependence. Figure 2.3 is therefore a valuable tool when it comes to analyzing and characterizing the self-propulsion velocity dependence of active systems.

2.8.1 Self-overlap order parameter

The self-overlap function returns a Boolean value based on the displacement of a particle as a function of time. An example of the formulation of the self-overlap order parameter [30, 46] is

$$Q_t(\tau) = \frac{1}{N}\sum_{j=1}^{N} \omega(|\vec{r}_j(\tau+t) - \vec{r}_j(t)|, \delta). \tag{2.38}$$

Here $\omega(r, \delta)$ is the step function which is 1 when $r \leq \delta$ and 0 otherwise. The time average $\langle \ldots \rangle$ is calculated over the interval $t \in [0, t_{\text{sim}} - \tau]$, where t_{sim} is the total simulation time.

The function is called the self-overlap function, because it measures the particle overlap with itself as a function of time. A particle moving farther than δ in a time interval τ, i.e. an average velocity $v = \delta/\tau$, will have a Q_t-value of 0. A system with a collective velocity v will reach an average Q_t-value of 0 at $\tau = \delta/v$. The latter is a property of a free active-matter system.

2.9 Particle energy

For an active particle, two distinct types of energies can be defined. One is related to the velocity of the particle while the other is related to the repulsive potential of the system. Depending on the the setup of the system, mainly density and potential cut-off distance, one of the two types of energy can become zero. In low density systems there will be few of no forces between neighbouring particles, and the associated forces will be zero. In highly dense systems the particle may reach a jammed state, stuck in the potentials of neighbouring particles. In such cases the energy associated with the movement of particles will be close to zero, while the energy related to the potentials acting on the particle will be high.

2.9.1 Interaction energy

In an active system with particle-particle interaction, the proximity of other particles will generate a force. In the model presented, i.e. Equation (2.22), this force is derived from the particle-particle-interaction potentials. Corresponding to this interaction force, an interaction energy can be defined. For each particle this energy is only a function of the position of the other particles in the system. The interaction energy for a time t be calculated as,

$$E_{\text{pp},i}(t) = \sum_{i \neq j} V(r_{ij}(t)), \tag{2.39}$$

where $\vec{r}_{ij}$ is the distance between particle i and j, and the sum over all the particles in the system.

The interaction energy will result in movement of the particle, deformation (compression) of the particle or a combination of both. In a fully jammed system the particles will not move, and all the interaction energy from the neighbouring particles will go to deformation of the particle. In such a system, typically a highly dense system with repulsive particles, the interaction energy of each particle will always be positive, and rather constant. In systems with lower density the interaction energy will also contribute to the movement and altered velocity (w.r.t. the self-propulsion velocity) of the particle.

2.9.2 Kinetic energy

The kinetic energy of an object is defined as $E_\text{k} = \frac{1}{2}mv^2$. In the active particle model described by Equation (2.6), and the further derived equations, the mass is 0. As the particles are massless, the kinetic energy cannot be defined. However, the squared velocity is still a meaningful measure of the activity and motion in the system. For the active systems in this thesis the term ”kinetic energy” will be used for the squared velocity where the mass is omitted. The new, reduced expression for the kinetic energy becomes,

$$E_{\text{k},i}(t) = \frac{1}{2} v_i^2(t). \tag{2.40}$$

where $v_i(t)$ is the absolute velocity of particle i. For a free (non-interacting) active particle, the kinetic energy will only be specified by the self-propulsion velocity, i.e. $E_0 = \frac{1}{2}v_0^2$, for any t.

To compare systems with difference self-propulsion velocities it can be advantageous to use the normalized kinetic energy instead of the kinetic energy, defined as,

$$E_{\text{norm}} = \frac{E_{\text{k},i}(t)}{E_0}. \tag{2.41}$$

The equation is unit-less, and will equal 1 for all free active particles, regardless of the self-propulsion velocity.

As seen from the descriptions above, the interaction and kinetic energy have an overlap, which is the part of the interaction energy contributing to the velocity of the particle. Thus, there is not conservation of energy between the two forms, and energies should be evaluated individually. Of special interest in this thesis is the time dependent distribution of the kinetic energy.

2.9.3 Kurtosis of the kinetic energy

To extract more information from the kinetic energy, the kurtosis can be calculated. The kurtosis is defined as,

$$\kappa(t) = \frac{\langle (E_k(t+\tau) - E_k(t))^4 \rangle}{(\langle E_k(t+\tau) - E_k(t))^2 \rangle^2}, \tag{2.42}$$

where the average $\langle \ldots \rangle$ is over all times t in the simulation, and $E_k(t)$ is sum of the kinetic energy of all particles for at time t. Note that the mass of the particle does not contribute to the value of the kurtosis. The difference in kinetic energy in the time interval $[t, t+\tau]$ creates a distribution of this difference for a fixed value of τ. Each unique value of t corresponds to a sample from the distribution. This type of distribution gives a quantitative measure for the change of energy in the given time interval.

The kurtosis can be interpreted as a measure for the thickness of tails of a distribution. A high value of the kurtosis corresponds many occurrence of extreme cases related to the distribution of the variable in question. For the kurtosis of the kinetic energy, a high value means that there are many occurrences of low or high values of the kinetic energy, compared to the expectation value of the kinetic energy.

For a Gaussian distribution the kurtosis is 3. The kurtosis subtracted by 3 is known as the excess kurtosis, $\kappa_{\text{ex}} = \kappa - 3$. Values of the kurtosis less than 3 implies the distribution contains less and fewer extremities than the Gaussian distribution. An example of this is the uniform distribution ($\kappa = 9/5$). Kurtosis of values higher than 3 implies a distribution that contains more extremities than the Gaussian distribution. An example with high kurtosis is the Laplace distribution ($\kappa = 6$).

As stated before, the kinetic energy for a free active will always be $E_0 = \frac{1}{2}v_0^2$. For a system of such particles, the energy difference of a particle in a time interval τ will always be 0, and the kurtosis will therefore become zero. In a system with high ordering and close to uniform movement, the situation will be similar to that of a system of active free particles, and the kurtosis will be close to zero.

2.10 Crackling noise and Gutenberg-Richter law

Across many different types of systems, crackling noise occurs. Crackling noise is the phenomenon in which the energy of a system is slowly increased and the system responds with discrete events of a power law distribution of energies [50]. Some well known examples of crackling noise include: Two tectonic plates rubbing past another causing intermittent earthquakes [51]; slowly crumpled paper emitting intermittent sharp noises [52]; and the magnetization of a magnetic material in an external field changes in a series of jumps [53].

Systems exhibiting crackling can be both reversible and irreversible. Magnetization and demagnetization is an example of a reversible process where crackling noise appears, known as Barkhausen noise. When a magnet is cooled to its corresponding Curie temperature, the magnetic spins align in clusters of different domain sizes as discrete events, and hence crackling noise is apparent. By reheating the magnet, demagnetization occurs in the exact opposite manner, such that the process is reversible. An example of an irreversible process exhibit crackling noise is an avalanche. The magnitude and occurrence of avalanches varies in size and time, as typical for crackling noise. However, once an avalanche has occurred, the process cannot be reversed (Avalanches will be discussed further in Section 2.11.4).

The Gutenberg-Richter law describes a specific relation within crackling noise. Gutenberg and Richter examined earthquakes and found a general relation between the magnitude of earthquakes and the probability of their occurrence [51]. This probability distribution takes the form,

$$N_M = 10^{a-bM}, \tag{2.43}$$

where N_M is the number of occurrences of magnitude M. The power law shape of the distribution is fit with a proportionality constant b and an intercept a. The magnitude M is the logarithm of a measured amplitude, adjusted to a certain reference value. This amplitude refers to an energy. Examples of the occurrences of different earthquake energies and the Gutenberg–Richter law is seen in Figure 2.4.

By measuring for instance the time dependent energy of a system, the behaviour of the system can be compared to the Gutenberg-Richter law. For the active matter systems presented in this thesis, the energy magnitude will be defined as,

$$M = \log(E_{\text{norm}}). \tag{2.44}$$

Note that E_{norm} is not actually a measure of energy, but rather the redefined normalized kinetic energy based on the square of the velocity of the particles. The maximum value of this magnitude is 1, which is achieved when the velocities of the particle is identical to the self-propelled particle. A free active particle will have a magnitude of 1.

2.11 States of active matter systems

In classic thermodynamics there are four fundamental states of matter, i.e. solid, liquid, gas and plasma. The states are mainly determined by temperature and density of the system.

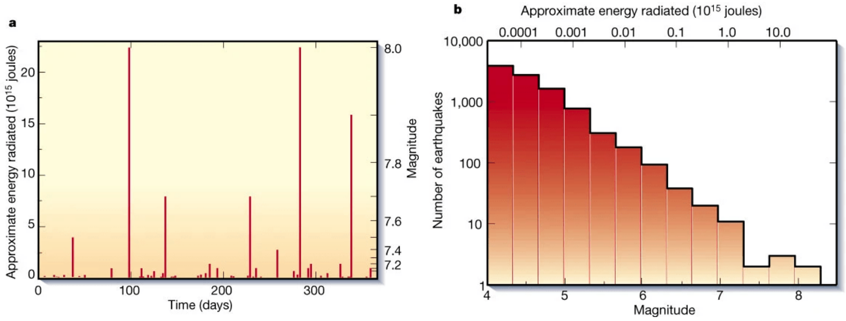

(a) Measured radiated energies form earthquakes **(b)** Histogram of numbers of energy mangnitudes

Figure 2.4: Gutenberg-Richter law for earthquakes measured in 1995. (a) shows the energy of earthquakes as a function of time. The energy distribution is discrete as typical for crackling noise. Some extremely high energies can be seen. (b) shows a linear decay of energies in the log-log space, as formulated by the Gutenberg-Richter law. The figures are reused from [50].

By altering these two parameters a system can undergo a phase transition between the states.

For active matter systems there are two more parameters defining the state of the systems, namely the activity and the persistent length the active particles. The activity is what has been described in this text as the self-propulsion velocity, and can be understood as measure of how much internal energy a particle will dissipate into the system. The persistent length is proportional to the rotational diffusion coefficient, as seen by Equation (2.11). Thus, with four parameters determining the state of an active systems, the definitions of the fundamental states of matter as no longer well defined.

This section will introduce some states of matter, and try to define them within the active matter framework. The expressions of the four fundamental states of matter will be used as a basis. However, be aware that these are only analogies to the equilibrium states and are not always clearly defined. The new states may only have some resemblance of the corresponding thermodynamic states. To make this difference more subtle the words ”active” and ”like” will be used to describe the new states, such ”active solid” or ”solid-like” state.

2.11.1 Solid

Solid states typically have high densities and low temperatures. In such a state particles will have difficulties finding pathways that allow movement over large distances. In a solid state the crowding from particle-particle interactions are larger than the energy injected at the particle scale. In other words, the particles are permanently trapped by their neighbours. The solid state can also be referred to as dynamical arrest. The individual particles do not have any kinetic energy, but the whole system can react as a homogenous block [54].

For a classic thermodynamic system the energy injected at the particle scale is the movement of the particles due to their thermodynamic fluctuations. For active particles this injected energy in the system also consists of the activity and persistent length of each particle.

Crystal

Simple systems, typically assemblies of identical particles in thermal equilibrium, will easily crystalize at high densities. In a crystal the particles are in dynamical arrest and long-range structuring can be observed. A crystal can be created by slowly cooling down or slowly increasing the density of the system. As the kinetic energy of the particle slowly vanishes, the system will gradually reach a steady state with minimal potential energy.

An active crystal or crystal-like state can be found in active matter systems as well. However, in addition to the requirements of the thermodynamic crystal, the activity must be sufficiently small and persistent length sufficiently large. Furthermore, the mixture and shape of the particle must be simple. Figure 2.5 shows an experimental example of an active crystal.

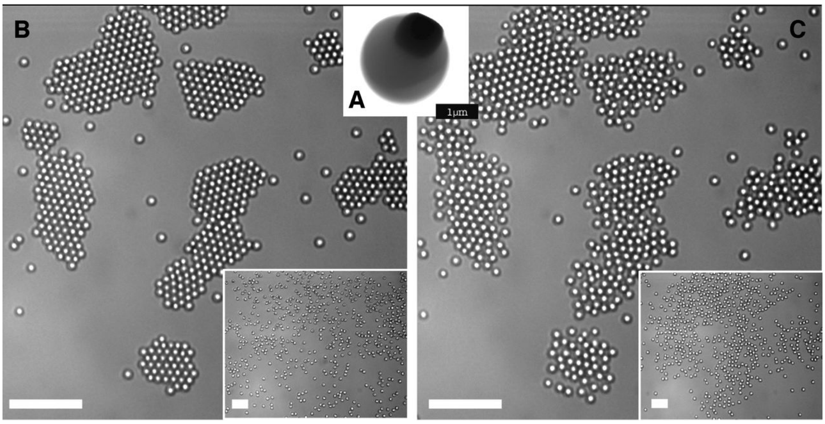

Figure 2.5: Active crystal under scanning electron microscopy. (A) A single bimaterial colloid. (B) Living crystals assembled from a homogeneous distribution (inset) under illumination by blue light. (C) Living crystals melt by thermal diffusion when the light is turned off, show for 10 s (inset, 100 s) after the light is turned off. The figure is reused from [10].

Glass

A glass can be defined as the phase where an equilibrium fluid has transitioned into an arrested amorphous state [55]. An amorphous state is characterized be the lack of long-range ordering and structuring of the particles. A glass is different from other amorphous state by its transition from a liquid phase. In comparison to the creation of a crystal, the glass transition is caused be a rapid change in dynamics. This rapid change can be observed in systems where the viscosity increases many orders of magnitude as the density or temperature of the system is changed by a small amount [56, 57]. The systems entering a glass state typically consist of more complex particle shape and composition. The rapid arrest of the particles on creation of a glass will lock particles in stressed states, that are not observed in a crystal.

The glassy behaviour describe here has also been observed in active matter systems, such as confluent epithelial cell sheet [58] and the biological process of vertebra body axis elongation [59]. In the forming of active glasses, the fluctuations due to temperature is negligible, and the activity and persistent length of the system acts as an effective temperature. For no activity the particles will be at full dynamics arrest. As the activity is increased the particles may start to diffuse and undergo interesting dynamics for a finite level of activity.

2.11.2 Jamming

As seen from the two previous subsections, dynamical arrest can arise from the lack of energy injected into the system. The arrest is solemnly related to the energy of a particle. In classical physics jamming is a specific state of dynamic arrests which occurs in nonbiological particulate systems when the packing density is increased above a critical threshold [60]. Jamming is a well known phenomenon in traffic, but has also been observed in smaller active systems such as mesenchymal tumor cells [61], collective cellular motion in a monolayer [62]. Figure 2.6 shows epithelial tissue migrating in a spatially heterogeneous manner. In parts of the system jamming occurs, while in other parts the particles are free to move.

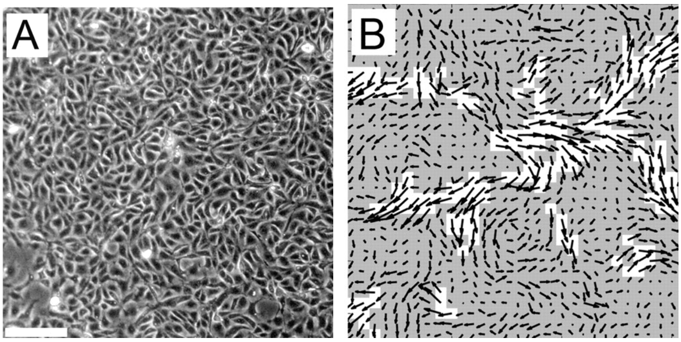

(a) Depiction of tissue **(b)** Velocity plots

Figure 2.6: Observed partly jamming in epithelial tissue. (a) shows a picture of the tissue under a microscope. (b) depicts the velocities of each tissue cell as arrows. The gray area represents (or at least close to) dynamical arrest. The figures are reused from [58].

For active systems the density of the system is often related to the self-propulsion velocity of the particle, not only the size of the system. Therefore, the glass transition phenomenon and the jamming phenomenon may have a partly overlapping definitions. In active matter studies, both terms are used to describe similar states of dynamical arrest. In this thesis the term jamming will be used related to the packing fraction of the system, while the term glass transition will be used related the self-propulsion velocity of the system.

2.11.3 Liquid

A classic liquid is a nearly incompressible fluid with constant volume independent of pressure. The individual particles are free to move around within the liquid, where their mobility is dependent on the temperature of the system. As with the classic liquid, the particles in an active liquid are not fixed to a certain position within the system. However their movements is not only related to their thermodynamical fluctuations but also the the self-propulsion velocity and persistent length of the particles.

Active liquids exhibits many traits not observable in classic liquids. Solon et al. [27] showed that pressure is not a state function for generic active fluids. Further, for active systems of low density, high local differences in density can be found. This is in contrast to classical thermodynamics where the fluctuations reduce as $1/\sqrt{N}$, following the central limit theorem. This phenomenon is know as giant number fluctuations, and is an interesting property of some active matter systems such as flocking, coherent motion and large-scale inhomogeneity [63].

Liquid crystal

In classical physics, liquid crystals is a state which flows like a liquid, but has some crystal-like properties, such as the structuring of the particles or ordering of the particle orientations. Active-liquid crystals have the same properties, but in addition the activity of the particles can govern the structure and orientation of the particles. An example is active particles with an elliptical shape, where ordering of particle orientations in a liquid state has been observed [63].

In active systems with significant nematic particle-particle interactions the particles will tend to align parallel or antiparallel. This creates long strand of particles moving in the same direction. For such systems liquid crystals may occur. The same will hold for polar particle-particle interactions, but here the particles will only align parallel.

2.11.4 Intermittency

Intermittency is described as the alternation of phases of periodic and chaotic dynamics [64]. The alternation can be either periodic or random. For systems exhibiting intermittency the characteristic order parameter often has a distribution as for crackling noise. For active systems, intermittency can occur as tension is built up over time in a steady state, which then is released through a chaotic event. As an active matter system is a non-equilibrium system with constant input of energy, the build up of stress following intermittent events seems inherent. Intermittency is not a state itself but rather a fluctuation between different states and is therefore an indication of critical dynamics.

Dislocation avalanches

Dislocation avalanches is a type of intermittency consisting of discrete event where defects in a system is reorganized collectively. Avalanches often occur near an unjamming transition [65], and has been observed in many types of systems such as the motion of dislocations in crystalline solids [66], the rearrangements of particles at yielding in amorphous materials [67], and granular matters including grains and bubbles [68].

The avalanches are often due to build up of stress in the systems which at some point is suddenly released. Afterwards, the particles return to dynamical arrest. The type of motion the particles follow in know as slip-and-stick motion. Avalanches can typically be found in systems with spatial heterogeneity, i.e. a large value of the four-point susceptibility function.

Chapter 3

Numerical Methods

The system of active Brownian particles described in Section 2.5 quickly becomes quite complex and is not analytically solvable with increasing number of particles in the system. This motivates the use of numerical methods to simulate such systems. Using numerical simulations the time evolution of the system can be estimated.

3.1 Discretization

3.1.1 Integrating the equations of motion for a free particle

The theory described in the Chapter 2 can be solved numerically by discretizing the equations of motion with respect to time. The first step is to define

$$t_n = n\Delta t, \tag{3.1}$$

where Δt is the size of the time step and n is the number of temporal steps needed to reach the time t. In the rest of this chapter, the subscript n implies that the corresponding variable is discretized. In previous studies the most prevailed method for integration of differential equations has been the Euler's method, or rather The Euler-Maruyama (EM) method [69] due to the stochastic diffusion term. Adapting Equations (2.6), (2.7) and (2.8) with this first order integration method gives

$$\vec{r}_{n+1} = \vec{r}_n + \Delta t v_0 \vec{u}_n, \tag{3.2}$$

$$\theta_{n+1} = \theta_n + \sqrt{2D_r\Delta t}\mu_n. \tag{3.3}$$

$$\vec{u}_n = \cos\theta_n\hat{x} + \sin\theta_n\hat{y}. \tag{3.4}$$

Here μ_n represents the discretized version of the distribution $\eta(t)$ at time t_n. Furthermore, μ_n satisfies $\langle\mu_n\rangle = 0$ and $\langle\mu_i\mu_j\rangle = \delta_{ij}$. From regular calculus one expects the noise term to be proportional to Δt, however with the use of Itô calculus this term is proportional to the square root of Δt. This ensures the normalization of the stochastic noise term is correct and makes the mean squared displacement equal for different time steps.

The recursiveness in Equation (3.3) can be written out to yield

$$\theta_{n+1} = \theta_0 + \sqrt{2D_r\Delta t}\sum_{i=1}^{n}\mu_i. \tag{3.5}$$

With the properties of the distribution function μ_n and Equation (3.1) the expectation value of the squared angle of orientation can be shown to be

$$\langle\theta_{n+1}^2\rangle = 2D_r\Delta t\sum_{i=1}^{n}\sum_{j=1}^{n}\langle\eta_i\eta_j\rangle = 2D_r\Delta t n = 2D_r t_n, \tag{3.6}$$

which yields a discretized representation of Equation (2.14). This numerical implementation of an free active Brownian particle can be compare to the analytic expectation value to ensure correct behaviour of the system.

3.1.2 Boundary conditions and particle-particle interaction

The introduction of boundaries and particle-particle interaction in the system will add corresponding force terms to the discretized equations presented in the previous subsection. The Euler-Maruyama integration scheme together with (2.22) and (2.23) gives,

$$\vec{r}_{i,n+1} = \vec{r}_{i,n} + \Delta t\big(v_0\vec{u}_{i,n} + \big(\vec{F}_{\text{b}}(\vec{r}_{i,n}) + \sum_{j\neq i}\vec{F}_{\text{pp}}(\vec{r}_{ij,n})\big)/\gamma_t\big), \text{and} \tag{3.7}$$

$$\theta_{i,n+1} = \theta_{i,n} + \sqrt{2D_r\Delta t}\mu_{i,n} + \Delta t\big(\Gamma_{\text{b}}(\vec{r}_{i,n}) + \sum_{j\neq i}\Gamma_{\text{pp}}(\vec{r}_{ij,n})\big)/\gamma_r. \tag{3.8}$$

with the parameters defined as in the previous chapter, but now replaced by a discrete representation. The index i represents particle number.

3.1.3 Adams-Bashforth integration for equations of motion

Adams-Bashforth (AB) integration routine [70] is a linear multi-step method where the information from previous time steps can be used to gain numerical accuracy. In this thesis the 2 step version (AB2) of the Adams-Bashforth scheme will be elaborated. It is easily adaptable for the system of interest as all the prefactors of the stochastic term μ are constants, but the general case is more complicated [71]. For increased readability the following parameters are defined,

$$\vec{\mathcal{R}}_{i,n} = v_0\vec{u}_{i,n} + \big(\vec{F}_{\text{b}}(\vec{r}_{i,n}) + \sum_{j\neq i}\vec{F}_{\text{pp}}(\vec{r}_{ij,n})\big)/\gamma_t,$$

$$\Theta_{i,n} = \big(\Gamma_{\mathrm{b}}(\vec{r}_{i,n}) + \sum_{j \neq i} \Gamma_{\mathrm{pp}}(\vec{r}_{ij,n})\big)/\gamma_r.$$

With these definitions the AB2 method is

$$\vec{r}_{i,n+1} = \vec{r}_{i,n} + \Delta t \bigg(\frac{3}{2} \vec{\mathcal{R}}_{i,n} - \frac{1}{2} \vec{\mathcal{R}}_{i,n-1} \bigg), \tag{3.9}$$

$$\theta_{i,n+1} = \theta_{i,n} + \sqrt{2D_r \Delta t} \mu_{i,n} + \Delta t \bigg(\frac{3}{2} \Theta_{i,n} - \frac{1}{2} \Theta_{i,n-1} \bigg). \tag{3.10}$$

AB2 compared to EM is more responsive to changes in the integrand in the equations of motion, i.e. the right hand side of Equation (2.22) and (2.23). The algorithm extrapolates the current trend based on different weighted samples from the two previous time steps. Other integration methods have been used in active matter simulations. A couple of examples are the Verlet integrations scheme [72, 30] and Heun's method [73]. This thesis will focus mainly on the EM method, although the error is known to increase significantly as enough time passes. A simple benchmark for the EM and AB2 method can be found in Appendix A. The EM method is chosen instead of the AB2 method as it is straightforward to implement the method and validate the results. The method is commonly used for active matter simulations [74, 75].

3.1.4 Uniform probability distribution

The stochastic noise in the orientation of the particle is represented by a uniform random distribution. The interval of this distribution must be chosen in such a way that requirements imposed by Equation (2.9) and (2.10) are met. For a uniform distribution in the the interval $[-a, a]$, symmetric around the origin, the probability density is defined as

$$P(\mu) = \begin{cases} \frac{1}{2a}, & \text{if } -a \leq \mu \leq a, \\ 0, & \text{else.} \end{cases} \tag{3.11}$$

This obviously meets the first requirement where the expectation value of the distribution should be zero.

The second requirement is $\langle \mu^2 \rangle = 1$ which imposes a restriction on the value a. By integrating the probability density squared the following expression is acquired.

$$\langle \mu^2 \rangle = \int_{-a}^{a} d\mu P(\mu) \mu^2 = \int_{-a}^{a} d\mu \frac{\mu^2}{2a} = \frac{a^2}{3} = 1. \tag{3.12}$$

This implies that $a = \pm\sqrt{3}$. This gives a uniform probability distribution in the interval $[-\sqrt{3}, \sqrt{3}]$.

3.1.5 Derived quantities

In order to analyze an active matter system different mathematical tools can be utilized. As seen from the previous chapter the self-overlap function, four-point susceptibility function and kurtosis will be used. All the aforementioned quantities rely on the time interval $[t, t+\tau]$. For each value of τ the average is created by iterating through all the discrete value of t in the dataset. Each value of τ must iterate through the whole data set. Thus, to achieve high resolution of the time interval is computationally demanding.

3.1.6 Initialization of system

The initialization of the system is important in simulations of particles. If two particles are initially placed in close proximity to each other non-physical behaviour can occur as a result of numerical instabilities. Ideally, the particles show be placed homogeneously within the boundaries of the system. For a circular system or a quadratic system with a quadratic number of particles, this is quite simple.

For a system of arbitrary length L and hight H, the situation is more complicated. There is no simple formula to achieve homogeneously spaced particles. The solution of this problem used by the author consist of several steps. First, the particles are placed at random within the system boundary. Afterwards, a set of points with a much higher density then the particles is also placed at random within the system. These point acts as a density mesh for which the particles in the system use to relax their position. Each point in the mesh is ascribed to the closet particle. The particle is then relaxed to the center of the belonging mesh points. The process is iterated until a sufficiently homogenous distribution is achieved.

3.2 Numerical implementation

The numerical methods described in this section have been implemented in the programming language C, by the author. A compiled language was chosen in order to ensure sufficiently fast computational times. This was important in order to run large systems over notable time intervals. The implementation uses to GNU Scientific Library [76] to generate the random numbers in the stochastic diffusion term. The method used is the the Mersenne Twister which is a pseudo-random number generator [77].

For the calculation of derived quantities such as the order parameter, the time system averaged energy, the four-point susceptibility function and the kurtosis, Python was used with the library Numpy [78]. The plots and snapshots are generated using matplotlib [79] in Python and visualized with Tikz/Pgfplots [80] in LaTeX.

The calculation of the four-point susceptibility function requires detailed information about the system for time intervals ranging over several decades. This results in huge files of data, which are time consuming to read into memory when postprocessing data. To circumvent this bottleneck the author has implemented the use of hierarchical data format (HDF5) [81], which yields significant improvements.

Throughout the designated period of this master thesis considerable effort has been put into the creation of the simulation tool. The tool has been develop from scratch using the theories and numerical methods from the previous chapters. Both the core C-code[1], and the code for postprocessing and plotting in Python[2] can be found at GitHub.

---

[1] `https://github.com/edvardstu/Master_Thesis_c.git`

[2] `https://github.com/edvardstu/Master_Thesis_python.git`

The simulations presented in the next chapter has been executed on a MacBook Pro with a Intel® Core$^{\text{TM}}$ i7-4870HQ CPU @ 2.50GHz × 8 processors and 16 GB of RAM running an Ubuntu Linux distribution. For a system size of 1000 particles with 2000000 time steps the execution time is approximately 50 minutes and generates approximately 2 GB of data. As of now the numerical method is only implemented to run in serial.

The main bottleneck of the current implementation is the particle-particle interactions. The current method for determining which neighbouring particles to interact with, is by iterating over all particles in the system and determining if the relative distance is smaller than a given threshold. This implies that the execution time of the code will scale as $\mathcal{O}(n^2)$, where n is the number of particles in the system. In other words this means that a doubling the number of particles will quadruple the execution time of the simulation.

Chapter 4

Results and Discussion

4.1 System setup

This chapter will mainly analyse and discuss a two dimensional system with periodic boundary conditions, harmonic potential for the particle-particle interaction force and with, and without the flying XY-model for the particle-particle torque. The physical parameters are listed in Table 4.1 and simulation parameters for the systems are listed in Table 4.2. These values will be used in all the following results. Some values in the table are denoted as ”-”, which implies that these values will be varied in the simulation.

Table 4.1: Free variables in the physical model for an active matter system with periodic boundary conditions, harmonic potential for the particle-particle force and the flying XY-model for the particle-particle torque. The values denoted in the third column is assumed for all following simulations and the notation ”-” implies the variable will be varied in the results.

Quantity	Symbol	Value
Self-propulsion velocity	v_0	-
Rotational diffusion coefficient	D_r	10^{-3}
Particle radius	r_a	0.5
Translational friction coefficient	γ_t	1.0
Rotational friction coefficient	γ_r	1.0
Harmonic potential strength	λ	20.0
Coupling strength of XY-model	γ	-

From Table 4.1, the self-propulsion velocity v_0 and the coupling strength of the XY-model model γ are of main interest and these will be varied through the simulations to come. The rotational diffusion coefficient D_r is chosen such that the stochastic nature of the system does not dominate over the particle-particle interactions for the given self-propulsion velocities. The harmonic potential strength λ is tuned to ensure a particle radius of $r_a = 0.5$ according to the discussions in Section 2.5.3, for a reference self-propulsion velocity of 1.0. The chosen harmonic potential strength also keeps the particles from ”traveling through” each other. The friction coefficients are simply set to 1.0, as they will not be of interest in this thesis.

Table 4.2: Free variables in the simulation program for the active matter system. The values correspond to a high packing fraction.

Quantity	Symbol	Value
System length	L	25.0
System height	H	25.0
Number of particles	N	1000
Number of time steps	n	$2 \cdot 10^6$
Time step	Δt	0.005
Particle-particle cutoff radius	r_c	1.025
Uniform distribution limit	a	$\sqrt{3}$
Self-overlap distance	δ	0.3

In Table 4.2 the number of particles N is set to 1000 due to computational restraint. As the critical point of the system is of interest (as will be seen in the results to follow) long simulation times are needed to fully characterize the system. For more than 1000 particles, this would lead to very long computational times. The size of the system L and H gives a high packing fraction of the system. The large number of time steps n gives a good data basis and is important for the transient behaviour of the system, as will be presented later in the thesis. The time step Δt has been optimized for the system setup. For further justification, see Appendix A. The particle-particle cutoff radius r_c is chosen close to twice the size of the particle radius, to ensure correct particle radius related to the harmonic potential. Section 3.1.4 explain the calculations of uniform distribution limit a. Lastly, the self-overlap distance δ is tuned according to the packing fraction and self-propulsion velocity of the system.

The periodic boundary system is initialized with the particles uniformly distributed inside the confinement with the particle direction θ chosen randomly. This implies that the system is in a highly chaotic state and each particle will experience much more interactions than in a steady state. To compensate for this fact, the interaction forces and torques are initially scaled down to zero and gradually increased to their nominal values. For a time step of $\Delta t = 0.005$ the first 1000 steps are used to gradually turn on the interactions. This is purely an numerical effort to stabilize the integration scheme and does not have a direct physical link. However, some analogies may be made. A similar effect could be achieved by either slowly increasing the self-propelled velocity of the particles or by starting out with a large system, and gradually decreasing the system size. These are system quantities that are possible to alter in actual physical systems.

4.2 Simulation results

In the two following sections the self-propulsion velocity will be systematically varied, while keeping the other parameters as defined in Tables 4.1 and 4.2 constant. Two values has been chosen for the coupling strength of the XY-model model, with $\gamma = 0$ in Section 4.2.1 and $\gamma = 0.1$ in Section 4.2.2. The goal is to characterize how the system depends on the self-propulsion velocities and the coupling strength of the XY-model.

For circular particles of radius $r_a = 0.5$, the packing fraction of the system is calculated to be 1.257 with Equation (2.29). This value is much higher than the random packing fraction of 0.82 [36], which implies that every particle is always interacting with its surrounding particles.

The chosen packing fraction can be compared to the highest values used by Fily et al. in [31] who also uses harmonic potentials for particle-particle interaction. Mandal et al. in [30] uses a packing fraction (the term density is used in the paper) of 1.2 and a truncated Lennard-Jones potential. Although, the packing fractions are almost equal, the different potentials give rise to a difference in repulsion energy, given by Equation (2.39). The increase in repulsion energy as the inter-particle distance decreases is much higher for a truncated Lennard-Jones potential than the harmonic potential. The harmonic potential might have a larger gradient close to the cutoff radius, but the Lennard-Jones potential quickly surpasses this constant gradient as the relevant distance is decreased. This implies that particles in the truncated Lennard-Jones potentials are much more restricted than with the harmonic potential.

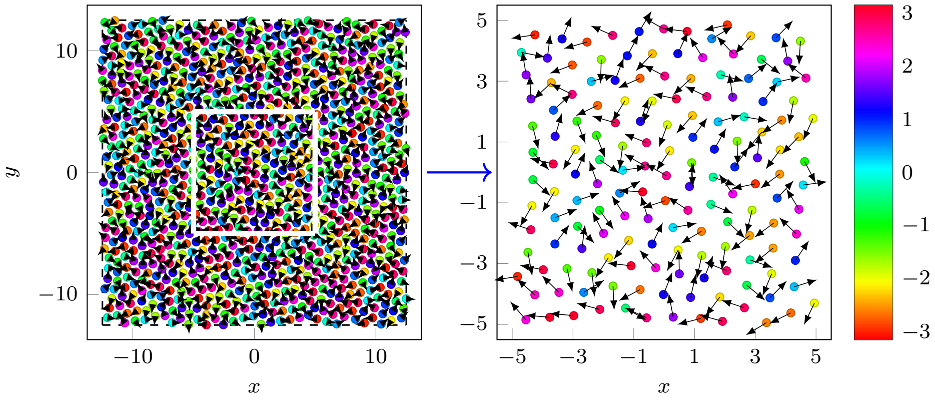

Figure 4.1: Snapshots of the particles at $t = 25$ with periodic boundaries. The left side shows the whole system, while the right side show the area marked in white. The color bar and the arrows indicate the orientation of the particle. The color bar range from $-\pi$ to π, and represent the polar angel of the particles. The particle size in not necessarily up to scale.

Figure 4.1 shows a snapshot of a system with $u_0 = 0.4$ and $\gamma = 0.0$ at $t = 25$. As the time elapsed is very short, the presented state could be the state of a system with any value of u_0 and γ. The system shows clear signs of the initial setup as the orientation of the particles are randomly distributed and the particles are distributed homogenously inside the boundaries.

4.2.1 Simulations with particle-particle force

The first simulation presented will be a system with no explicit particle-particle alignment torque. In other words, the coupling strength of the XY-model is $\gamma = 0$, which implies the term $\Gamma_{\text{PP}} = 0$ in Equation (2.23). The choice of γ also means that the shape of the particle is circular. However, the particle still has an orientation θ.

Figure 4.2 presents the time average self-overlap function, four-point susceptibility function and kurtosis of systems with different self-propulsion velocities. All the results are calculated from the time-dependent position, direction and velocity of each particle. The three quantities are plotted for one decade of self-propulsion velocity u_0. In general all the plots show a strong dependency of both the self-propulsion velocity u_0 and the time interval τ.

The self-overlap function, Equation (2.38), is plotted in Figure 4.2a. For all self-propulsion velocities, as the time interval τ increases the particle is decorrelated with respect to itself, i.e. the self-overlap function goes from one to zero. This behaviour is as expected for a system of particles in motion. The smaller the self-propulsion, the longer time a particle uses to travel the self-overlap distance δ. However, it is worth mentioning the that average velocity of the particles in the system is much lower than u_0, due to jamming. A rough estimate for the average system velocity for a given value of u_0 can be obtained by dividing the distance δ by time τ^* given be the first time value where $Q_t(\tau^*) \approx 0$.

Figure 4.2a shows that the self-overlap function decays as the time interval increases. As the values of the self-propulsion velocity increases the decay time of the self-overlap function decreases. The decay of $Q_t(\tau)$ in τ-log space shows the same kind of behaviour for all values of the self-propulsion velocity, except for $u_0 = 0.4$. Here, the decay is significantly faster than for the other self-propulsion velocities. This can be an indication that the dynamic in the region around u_0 differs from other values of u_0.

The four-point susceptibility function χ_4, given by Equation (2.37), is presented in Figure 4.2b for different values of the self-propulsion. This is the variance of the time averaged self-overlap function in Figure 4.2a. Therefore, χ_4 can be interpreted as the fluctuation around a given value of Q_t. By comparing the two figures it is apparent for the interval of τ where χ_4 has its largest values, Q_t changes value from 1 to 0.

For all self-propulsion velocities, χ_4 seems to follow a power law in the initial regime, as seen by a linear behaviour in the log-log space. By linear regression the gradients can be calculated, and the exponent μ of the power law t^μ is found to 2.29, 3.11, 2.86, 3.61, 4.81, 4.51, 3.98, 4.69 for increasing values of u_0. The gradients are calculated from the existing value of χ_4 and until the gradients of the curve has a dramatic change, either increasing or deceasing. For increasing values of u_0, the calculations of the gradients are based on a decreasing number of points. The latter gradients therefore have quite low precision.

In Section 2.8 and Figure 2.3 the behaviour of the four-point susceptibility function close to the critical temperature was discussed. In the initial time sector a gradient of 2 was associated with diffusive behaviour and a gradient of 4 with ballistic behaviour. Further the intermediate time sectors of Figure 2.3 disappears for low temperatures. Comparing this to Figure 4.2 indicates that at low values of self-propulsion velocities the particles has a diffusive behaviour for short time intervals and exhibits α-relaxation for longer time intervals. For larger values of self-propulsion velocity the gradient is larger than that of

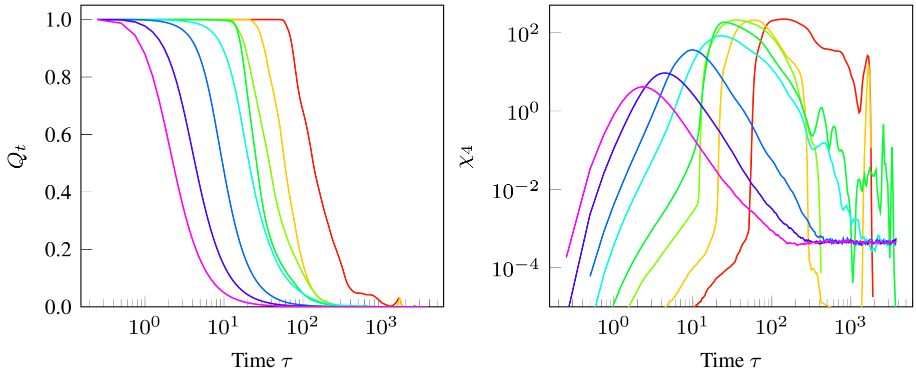

(a) Self-overlap function.

(b) Four-point susceptibility function.

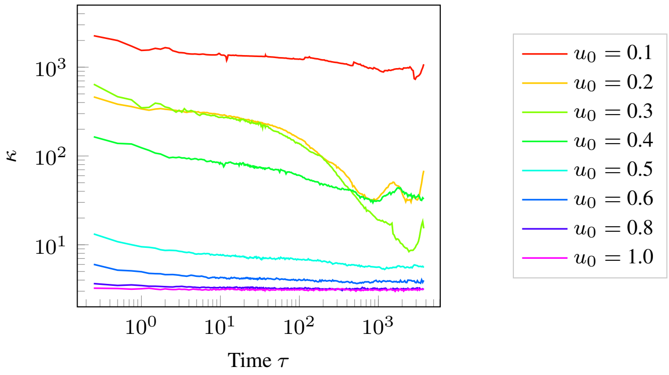

(c) Kurtosis of the spatial averaged particle energy.

Figure 4.2: Derived values of simulation with $\gamma = 0.0$, i.e. no directional alignment, with the simulations parameters in Table 4.2. (a) The order parameter $Q_t(\tau)$ shows a clear relation between the self-propulsion velocity and decorrelation of particle overlap. (b) The four-point susceptibility function $\chi_4(\tau)$ shows a large increase in the variance of the self-overlap function as u_0 approaches 0.4 from below, which indicates a change in behaviour of the system. In (c) the self-propulsion values of $u_0 = 0.2$, 0.3, 0.4 the kurtosis $\kappa(\tau)$ exhibits large changes with with increasing time τ.

diffusive behaviour as the alpha regime is reached. From Figure 2.3 this behaviour can either be categorized as a ballistic or late beta regime. As there are quite few data points for short time intervals it is not possible to observe whether the intermediate regimes has collapsed, and furthermore it is not possible to conclude which regime is present for high value of self-propulsion velocities.

As with the plots presented of Q_t, the four-point susceptibility function for $u_0 = 0.4$ stands out. The well-defined increase in gradients seen for low self-propulsion velocities are noe longer visible. The transition over to the alpha regime becomes smoother and the gradients increase significantly around this value. This change also indicates that the dynamics of the system for short time intervals changes significantly with the self-propulsion velocity. The change from a diffusive to ballistic behaviour is an argument for a transition from an arrested particle, to a particle with free-particle like behaviour in a limited time interval.

The kurtosis described in Equation (2.42) is presented in Figure 4.2c. The values of the kurtosis give a measure for how much the distribution of energy difference for the whole system in a time interval τ deviates from the Gaussian distribution. As the values of u_0 increase, the kurtosis approached 3 for all τ-values. This is an indication that the particles have an free-active-particle-like behaviour when the self-propulsion is large enough. Note that this free-active-particles-like behaviour is still subject to particle-particle interaction which will cause an effective self-propulsion velocity different from the one for an actual free-active particle.

As the self-propulsion is increased, the kurtosis is observed to gradually decrease. There are no distinct jumps in the values. This stepwise decrease in κ implies that the transition from an arrested particle to the free-particle-like behaviour, discussed previously, is happening gradually. For small self-propulsion velocities the value of κ is large. This means that the systems have many events far from the average of the system. This behaviour can for instance be found in a fully arrested system where only a few particles occasionally move. In such a system an increase in motility of the particles would results in smaller values of κ. This is the effect expected from increasing the self propelling velocity in an arrested active system.

The strong τ dependency of kurtosis for intermediate self-propulsion velocities can be used to deduce characteristics about the transient behaviour of the system. For short time intervals the kurtosis shows large values, which as mentioned, is found in a dynamically arrested state. Assuming this is the state of the system, a decrease in κ as the time interval is increased, point towards and increase in movements of particles in the system which does not manifest at short time intervals. In other words, The sum of all the extreme deviations observed at short time intervals will over longer time intervals appear as free-active-particle-like behaviour.

To further investigate how the system depends on the value of u_0, the four-point susceptibility function is studied in greater detail. Additionally, the initial values of the excess kurtosis κ_{ex} are plotted in Figure 4.3.

Figure 4.3a shows a rescaled version of the four-point susceptibility function. The time interval τ is converted into a length unit $u_0\tau$, a unit for how far a free particle with velocity u_0 would travel in the time interval τ. The rescaled four-point susceptibility function shows an interesting u_0-dependency. As u_0 is decreased from 1.0, the peak of χ_4 increases

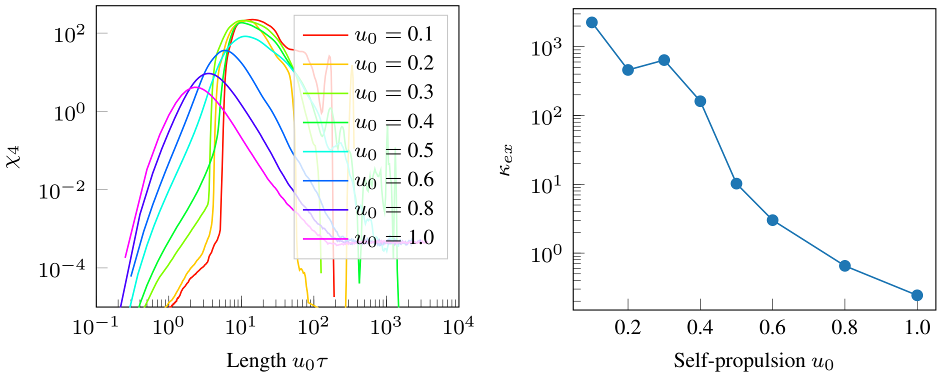

(a) χ_4 for rescaled axis. **(b)** Excess kurtosis $\kappa_{\text{ex}}(\tau = 0+)$.

Figure 4.3: Values derived from Figure 4.2. (a) The four-point susceptibility function from Figure 4.2b, for the x-axis rescaled to $u_0\tau$, where a clear data collapse is visible for small values of the self-propulsion velocity. (b) $\kappa_{\text{ex}}(\tau = 0+)$ where $0+$ is the smallest store time interval which is $50\Delta t$. A point of inflection can be found between 0.4 and 0.5. if the data point of 0.2 is disregarded.

in value and moves towards larger time intervals. As u_0 reaches 0.4 the peak stops moving and the peaks of the remaining velocities collapse into one point. As stated previously, the particles in the system does not move with self-propulsion velocity u_0, and thus the author has not found a physical explanation of the characteristic length associated with the peaks in χ_4. Nevertheless, the collapse of the peak at low self-propulsion velocities imply similar dynamics for small velocities, and as the self-propulsion velocities exceed 0.4 the dynamics of the system start to change.

The excess kurtosis $\kappa_{\text{ex}}(\tau = 0+)$ as a function of u_0 is presented in Figure 4.3b. The time interval $\tau = 0+$ represents the shortest possible time interval in the system, which due to simulation limitations is $50\Delta t$, the interval of which results are saved. The figure shows that the increase in excess kurtosis scales with the decrease in self-propulsion velocity. The rate of diminish with the increase in u_0. In the u_0-log space plotted the graphs shows a point of inflection close to $u_0 = 0.4$. According to Mandal et al. [30] the point of inflection of the excess kurtosis occurs on the phase boundary of an intermittent phase. The latter motivates a more detailed study of the spacial and temporal energy distributions in the system, especially for $u_0 = 0.4$.

In Figure 4.4 the energy of the systems with $u_0 = 0.4$ is presented. The data used to generate the energy plots result from the same simulations used in Figures 4.2 and 4.3.

Figure 4.4a shows the averaged normalized kinetic energy, Equation (2.41) as a function of time. The normalized energy is most of the time close to zero. At random times the energy spikes up to a maximum value of 0.02. In the time intervals with close to zero kinetic energy the particles are in a state of dynamical arrest, i.e. there is no, or close to no, movement. In this state of the system, the kinetic energy is significantly less than one percent of the self-propulsion of the equivalent free active particle. The figure shows close resembles to energies of earthquakes presented in Figure 2.4a.

From the sudden energy spikes in Figure 4.4a, it is apparent that the active particles

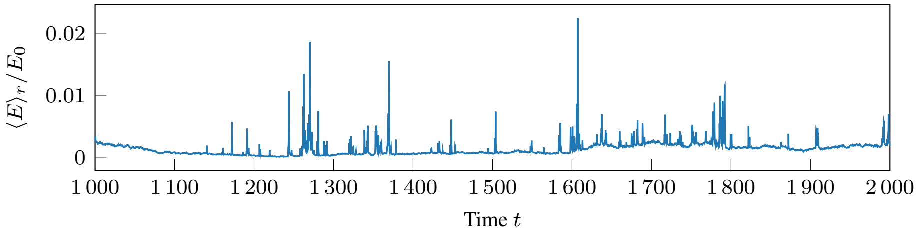

(a) Normalized kinetic energy in time interval $t = 1000$ to $t = 2000$ (Total simulation time is $t = 10^4$).

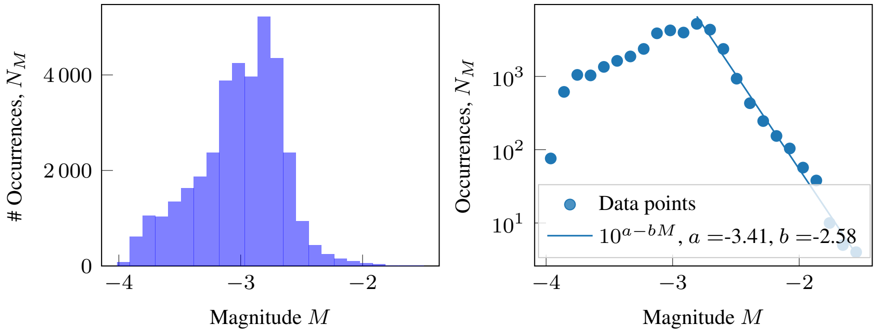

(b) Histogram of the magnitude of energies.

(c) Gutenberg-Richter law for magnitudes.

Figure 4.4: Several representations of the calculated normalized kinetic energy of the system in Figure 4.2 for $u_0 = 0.4$. (a) shows the averaged system energy normalized by the self-propulsion velocity as a function of time. Several intermittent spikes in energy is apparent. (b) and (c) show the number of occurrences of each magnitude of energy, i.e. the logarithm of the normalized kinetic energy. In (c) the Gutenberg-Richter law is presented as a solid line. The law is fit using linear regression in the log-log space with a starting point at the highest number of occurrences.

move in bursts of short time intervals, before returning to a state of dynamical arrest. As presented in Section 2.11.4 this is a characteristic behaviour for intermittency. Both the magnitude and duration of the events vary in size. The intermittent event observed here is in agreement with the results presented by Mandal et al. [30] for dense active matter systems with hard repulsion Lennard-Jones potential.

The variation of energy in the system is clearly seen from histogram in Figure 4.4b. The histogram shows the number of occurrences of a certain energy magnitude, as given by Equation (2.44). Note that the histogram is generated from the whole simulation time $t \in [10^3, 10^4]$, as compared to Figure 4.4a. The measure of magnitude along the x-axis is divided into 24 bins. The spread of energy ranges more than two decades. The weight of energy is around, or a bit below the center of magnitudes. Only a handful of energies reach up to magnitudes M of -2 ($E_{\text{norm}} = 0.01$) or higher, corresponding to the spikes in Figure 4.4a.

Figure 4.4c shows the values of histogram on a logarithmic y-axis plotted along with a fit of the Gutenberg-Richter law, Equation 2.43. The logarithmic values of the histogram resemble the occurrences of energies shown in Figure 2.4b. The fit is calculated by linear regression of the logarithm on the number of occurrences, $\log(N_{\text{M}})$ and the magnetite M.

Only magnitudes larger of equal to the magnitude corresponding to the largest number of occurrences are used. The fit parameters are found to be $a = -3.41$ and $b = -2.58$ with a standard error 0.079 for the estimation.

The good fit of the Gutenberg-Richter law for the high magnitude regime implies that the distribution of energy follows a power-law with high accuracy. Consequently, there are many occurrences of low energies, and only a few occurrences of high energies. A power-law behaviour for a system is commonly associated with critical dynamics of the system. For such a state, the parameter controlling the system has reached a critical point and often indicates a proximity to phase transition of the system [82].

In order to understand the nature of the energy spikes in Figure 4.4a, the energy magnitude of each particle for selected times t has been plotted in Figure 4.5. To distinguish different particle energies, the energy magnitude for each particle is represented by a color map, where dark blue is $E_{\text{norm},i} = 0.0001$ and bright yellow is $E_{\text{norm},i} = 1.0$. This means that dark particles in the snapshot are essential at rest compared to the particles that light up. Bright yellow colored particles have a velocity close to the self-propulsion velocity.

The largest peak in Figure 4.4a corresponding to a time of $t = 1607.25$. Figures 4.5a, 4.5b and 4.5c are snapshots of the system just before, during and just after the peak in energy, respectively. Just before the peak, the energy distribution in the system is almost homogeneous. As the peak occurs a bright spot lights up in the system. Outwards from the centre of the bright spot, the energy rapidly decline. The snapshot after the peak shows that the relatively large energy in the peak now as been dissipated to the neighbouring particles. As seen from Figure 4.4a its takes a certain period of time before the low energy state of the system is reached anew. This type of motion is commonly known as slip-and-stick motion. Some particles build up enough energy to detach, or slip, from the arrested part of the system. After a short while the energy is dissipated in the system, and the free particles now stick to the rest of the system again.

The bursts of movement for the system with $u_0 = 0.4$ occurs in avalanches, a seen by the sudden motion of several particles at once. During the avalanche the particles near the centre of the event has a energy close to 1.0 and therefore a velocity close to the self-propulsion velocity of the corresponding free particle. This high energy is only evident for a short period of time, before the particles are diffused. As seen from the snapshots, the energy spikes visible in Figure 4.4a is only caused by a fraction of the particles in the system. The relatively small normalized energy at the spikes are justified by the fact that the majority of the particles are at dynamical arrest.

Weeks et al. [49] states that in colloidal suspension near the glass transition, α-relaxation occurs by means of cooperative particle motion. In other word, when one particle moves, another particle moves by closely following the first. The intermittency events in 4.5 has this described behaviour. Therefore it is plausible that the intermittency events observed is the α-relaxation visible in the four point susceptibility function in Figure 4.2b.

From the figures presented up until now in this section, the state of the system for a self-propulsion value of $u_0 = 0.4$ is found to be an intermittent phase with well-defined avalanche events. The critical dynamics of the system points towards a potential phase transition [83], which encourage the identification of the states of the systems of u_0-values smaller and larger than 0.4.

Figure 4.6 shows histograms of the normalized kinetic energy, as described in Equation

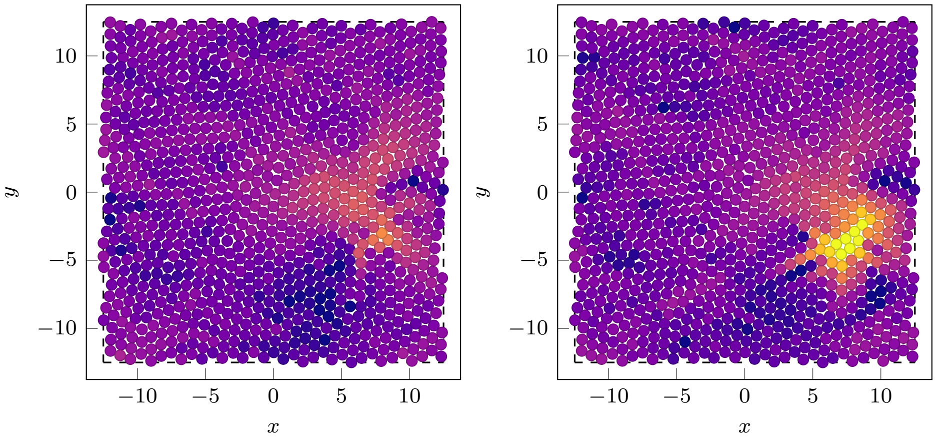

(a) Time t = 1606.75.

(b) Time t = 1607.25.

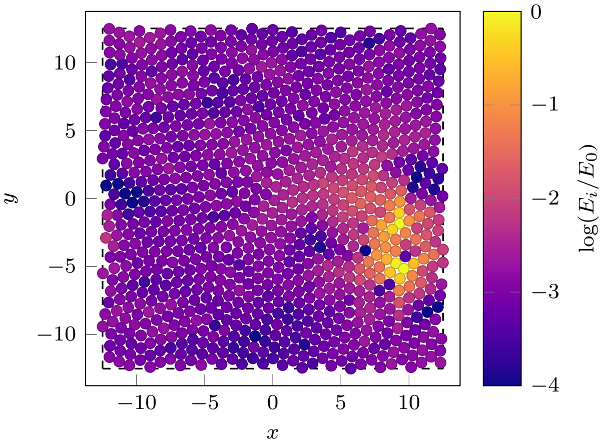

(c) Time t = 1607.75.

Figure 4.5: Snapshots of the logarithm of the normalized kinetic energy of particles with $u_0 = 0.4$. The snapshots take place (a) before, (b) during and (c) after an avalanche occurrence. The data is from the same system plotted in Figure 4.4. The bright cluster in (b) can be recognized as largest spike in Figure 4.4a.

(2.41). The self-propulsion velocity ranges from $u_0 = 0.1$ to $u_0 = 1.0$. The histogram are generated from the same simulations presented in the previous Figures 4.2 and 4.3. Note that the range of the axis are individual for each plot.

First of all, the histogram for $u_0 = 0.4$ is the same data as presented Figure 4.4c. The right half of this distribution was found to follow the Gutenberg-Richter law with high accuracy. By visual inspection the same kind of power-law decay for increasing magnitude can be seen for self-propulsion velocities values of 0.1, 0.2 and 0.3. Similar kind of behaviour can be found in these systems, where where low energies occur often and high energies occur rarely. As discussed earlier, this behaviour is characterizing for an intermittency, and it is therefore probable that intermittency can be found for self-propulsion (far) below $u_0 = 0.4$. However, as u_0 is decreased the histograms show that the occurrences of high energy values is reduced. This implies that the number of intermittency events is reduced along with the self-propulsion velocity.

As the self-propulsion velocities increase above $u_0 = 0.4$ the distributions of normalized energy presented in the histograms takes on the shape of a parabola. For a perfect parabola in the log-log space, the occurrences of magnitudes would have a normal distribution. For such a shape to occur, the particles are required to have a magnitude close to the average magnitude of the system. This type of behaviour means the the slip-and-stick motion of the particles has disappeared and that the particles are able to move much more freely around.

In Figure 4.6 the magnitude on the x-axis range from -4 og -1, i.e. a normalized energy in the interval $E_{\text{norm},i} = 0.0001$ to $E_{\text{norm},i} = 1.0$. The difference of average magnetite from low to high self-propulsion velocity is almost two decades. Thus, the average movement in the system is dramatically different, where the system with high self-propulsion velocity has particles moving at average almost 10 times as fast as in the system with high self-propulsion velocity. This fact further suggests that a phase transition happens around $u_0 = 0.4$. The phase of the system for large self-propulsion velocities is hard to characterize from the histograms.

The distribution of energies in the histogram reflect the kurtosis presented in Figure 4.2c. For small values of the self-propulsion velocity the kurtosis has a large value, which is reflected by the long right-hand side tail of the respective histograms. For $u_0 = 1.0$ the histogram has an approximate shape of a parabola which indicates a Gaussian distribution of the energies. This is compliant with a kurtosis close to 3.

To further identify the state at low and high self-propulsion velocities the time dependent average energy and snapshots of energy state will be presented. Figure 4.7 show the energy of the self-propulsion velocity equal to 0.1, 0.5 and 1.0.

The top plot in Figure 4.7 show the energy of the system for a self-propulsion velocity of 0.1. The plot is rather similar to 4.4a, but the spikes occur less frequently. This is supported by the corresponding histogram in Figure 4.6, where the occurrence of high energies is seldom. Since there are only two energy bursts visible in the top plot in Figure 4.7, it implies that the data in the histograms in Figure 4.6 might be lacking for small values of u_0. It seems that even for very low values of self-propulsion velocity intermittency occurs, and it is expected that the histogram should follow the Gutenberg-Richter law, as with $u_0 = 0.4$. One could speculate that the accumulation of much more data would results in this kind of behaviour. The observation of intermittency for small self-propulsion

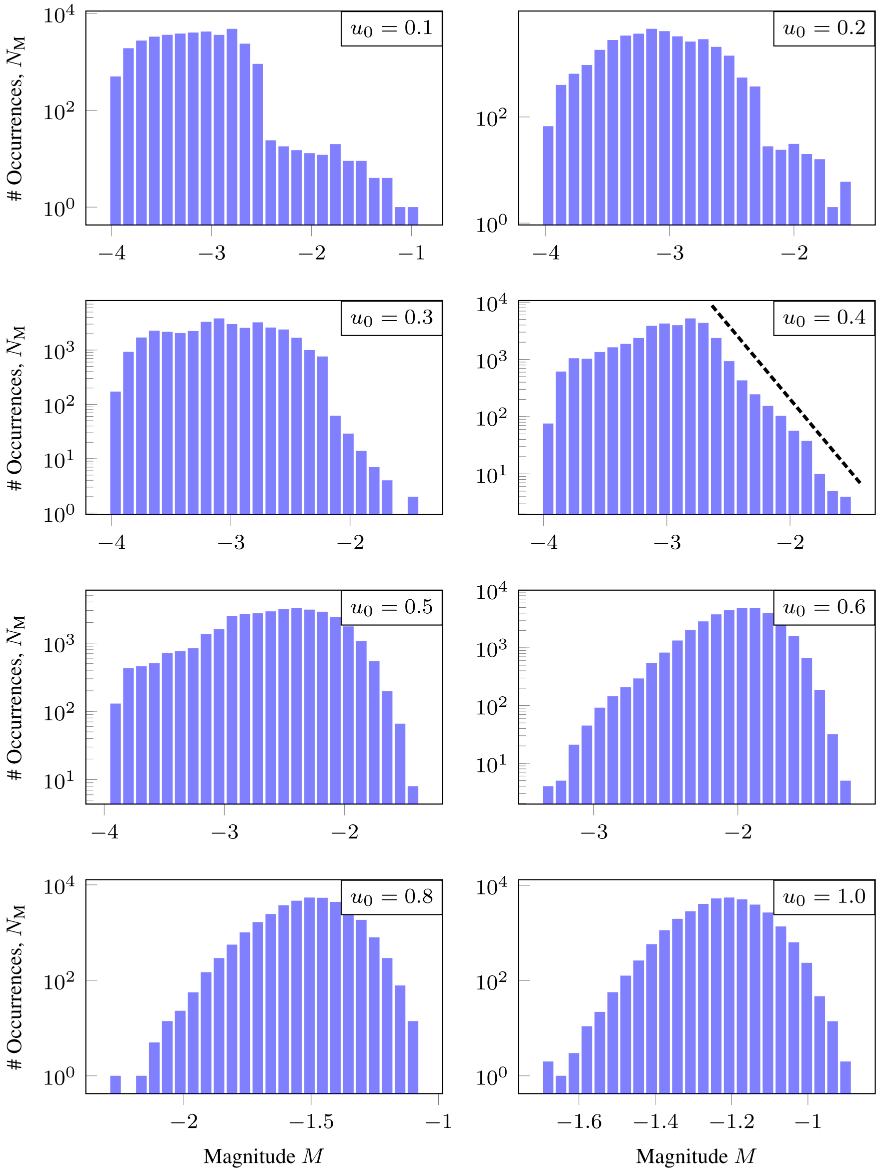

Figure 4.6: Histograms of normalized kinetic energy, Equation (2.41), for periodic systems ranging from $u_0 = 0.1$ to $u_0 = 1.0$. The histograms are generated from the same simulations as Figure 4.2. As the self-propulsion is increased the weight of normalized energies shifts to the right, i.e. to higher energies and the lower bound of the normalized energies increase. For $u_0 = 0.4$ the system starts to flow corresponding to the critical point of the system. Further, the doted line represents the Gutenberg-Richter scaling law (see Figure 4.4c). The slope of the line is -2.58 in the log-N_m space. For the lowest velocities it is likely that the dataset is not sufficiently large to supply representative data of the high magnitudes.

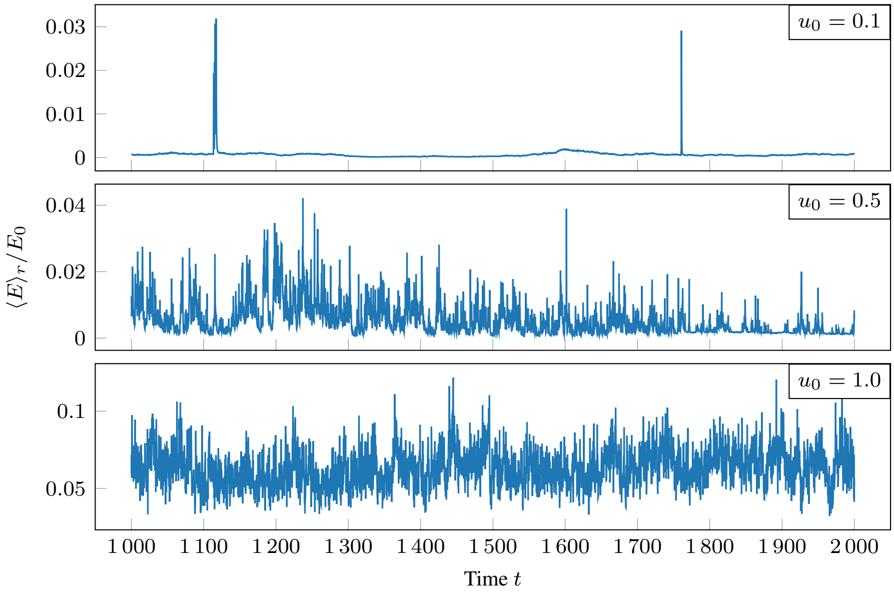

Figure 4.7: Average normalized kinetic energy as a function of time for different values of the self-propulsion velocity. For $u_0 = 0.4$ the system shows two distinct intermittency events, while for $u_0 = 1.0$ system-wide dynamical arrest is never observed.

velocities contradicts the results produced by Mandal et al. [30]. This could be because Mandal et al. use the truncated Lennard-Jones interaction potential, which is mucher harder than the harmonic potential or because they use a binary particle mixture, and not a single type of particle as in this thesis.

The middle plot in Figure 4.7 show highly frequent occurrences of energy bursts for a self propelling velocity of 0.5. Infrequently, the energy convergence towards zero and stays there for a finite amount of time, before the bursts continue. The system has intermittency events almost continuously, but goes back to full dynamic arrest for short time intervals. At these points it seems if most of the system is at rest, but there is always one region thats is in movement. There are at least two obvious explanation for these particle movements. The first one is a cluster of particles moving around, and the other is many separate intermittency events that overlap in time. Of course a combination of these is possible. In order to figure out how the particles move, the individual energy of the particles must be studied in greater detail.

The bottom plot in Figure 4.7 shows rapidly changing energy for a system with self-propulsion velocity of 1.0. In comparison to previously presented energy plots the system never has an energy of 0, and system wide dynamical arrest does not occur. However, there is no assurance that all the particles contribute to the kinetic energy of the system. On the other hand, as the average energy is roughly five times larger than that of the energy bursts in Figure 4.4a and the corresponding intermittency event in Figure 4.5b includes about 10-20 particle, one can suspect all the particles of the system to be in motion. This argument holds if all the particles in the system with $u_0 = 1.0$ has similar a energy to the 10-20 particles comprising the intermittency event for $u_0 = 0.4$. Figure 4.7 compares well the the energy of a liquid state presented by Mandal et el. [30].

Figure 4.5 shows snapshots of the periodic system for different values of $u_0 = 0.4$ at different times. The time is chosen in such a manner that intermittency events are visible, based on the energy peaks seen in Figure 4.7. For a system-wide dynamical arrest the whole system would take on the dark blue seen in large parts of Figure 4.8a.

In Figure 4.8a the energies of the particles in the system with $u_0 = 0.1$ are plotted. The event is very similar to the avalanche seen in Figure 4.5b for u_0. By visual inspection the size of the two avalanches appear rather equal in size, regardless of the former having almost 50% higher average system energy during the event. Again, this demonstrates that the systems exhibits intermittency events for low values of self-propulsion velocity. Whether this holds for all non-zero velocities cannot be determined from the simulations presented. However the trend points towards a faster than linear decrease in the probability of intermittency events to occur with the reduction of self-propulsion velocity. Furthermore, this suggests that at even lower self-propulsion velocities the intermittency events would still occur, but they would be most unlikely to observe.

Through the discussion presented up to now, it is clear that the self-propulsion velocity of 0.4 is close to the critical point of the system. As seen previously, well-defined single avalanches occur for this realization of the system. Figure 4.8b shows the a snapshot of the state of the system from a small increase in self-propulsion velocity, i.e. $u_0 = 0.4$. The small increase causes quite dramatic effects in the system. The previously well-defined avalanches has now been replaced with a more smeared out event, seemingly consisting of three epicenters. For this value of u_0 it seems the energy injected in the system by the active particles almost is enough to overcome the particle-particle-interaction forces causing dynamical arrest. This state looks similar to the partly jammed state presented in Figure 2.6b.

The occurrence of multiple intermediate events as observed here, will impact the energy distributions in the histograms seen in Figure 4.6. The histograms measure the occurrences of certain average system energies. When analyzing the histograms with power laws, each energy is assumed to belong to one single intermittency event. The histograms for high velocities will be biased towards high energies. Two small intermittency events would be recognized as one large event and therefore increase the right tail and also shift the body towards the right of the distribution. The impact is a left-skewness of the distribution. This skewness washes out the power law relation clearly seen for u_0, and the transition between a power law distribution to a Gaussian distribution may seem smoother than it actually is in the system.

Figure 4.8c shows the energies of the particles for $u_0 = 1.0$. The snapshot differs from previous snapshots as there is not one a well-defined single spot with increased energy, but rather a group distribution inside the system. Very few particles seem to be arrested, and from Figure 4.7 the average particle velocity is calculated to be approximately 25% of the self-propulsion velocity. The large movements, along with the high, imposed density in the systems are evidence of this being a liquid phase.

From the detailed and in-depth investigation of systems for different values of u_0, it seem that a slip-and-stick motion common for intermittency is a recurring observation. The frequency of these events increase with the self-propulsion velocity until single events

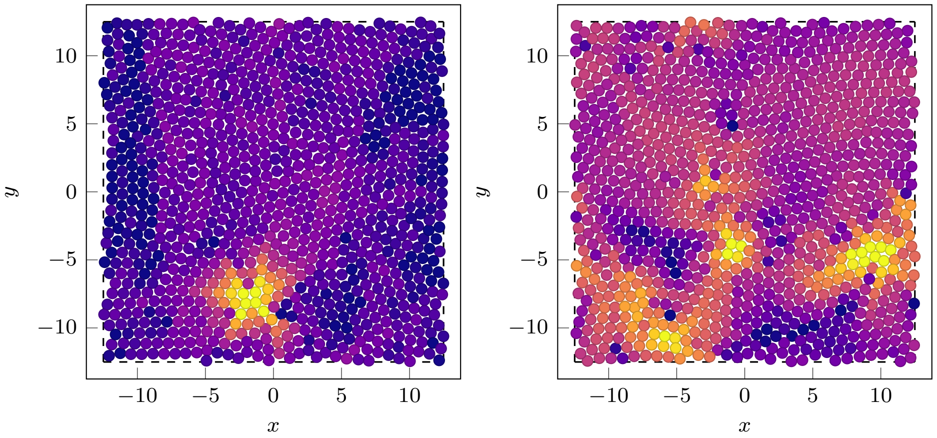

(a) $u_0 = 0.1$, t = 1760.75.

(b) $u_0 = 0.5$, t = 1237.25.

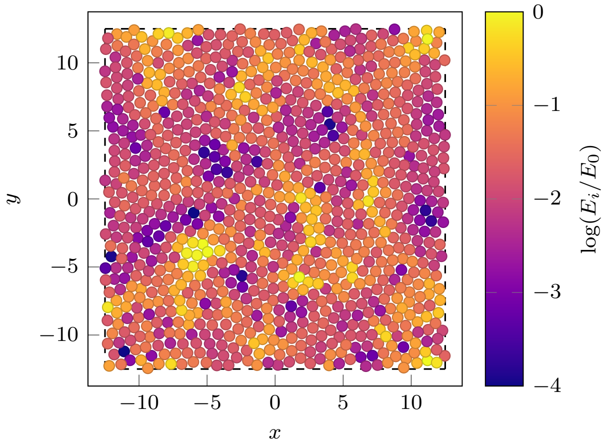

(c) $u_0 = 1.0$, t = 1761.25.

Figure 4.8: Snapshots of the logarithm of the normalized kinetic energy of particles for different values of u_0. The snapshots correspond to the system averaged energy in Figure 4.7. (a) second energy spike from the top plot, (b) highest peak from the middle plot and (c) randomly chosen time from the bottom plot. The number of intermittency events at one point in time increases with the self-propulsion velocity.

are no longer recognizable and the systems takes on a liquid-like phase.

For all the snapshots presented the system takes on a hexagonal pattern with defects. The degree of imperfections has not been measured, but by visual inspection the structure seems more periodic for small values of self-propulsion velocities (this could also be a visual misinterpretation as snapshots for larger velocities contain more colors). Anyway, such hexagonal patterns are well known to occur in crystals. The dynamically arrested state of the system can therefore be characterized as an active crystal and the liquid-like state as an active-liquid crystal. Other studies typically steer away from crystallization by using binary mixtures of particles [31, 54], such as the Kob-Andersen mixture [30, 84], which consist of two type of particles with different sizes and interaction-potential strengths.

In active matter physics the terms jamming and glass transition are both commonly used to described system undergoing a transition to dynamical arrest. In the framework of active matter physics, Berthier et al. [54] describe jamming as a zero-temperature and zero-activity transition merely caused by the geometry of the system. However, the glass transition phenomenon is described as a competition between the crowding, i.e. the inter-particle force, acting on a particle and the activity or self-propulsion of the particle itself. In terms of these definitions, the transition observed in this system is similar to the glass transition. As stated, the arrested state of the system take on a hexagonal structuring, reminiscent of a crystal, and it would therefore be unnatural to identify the arrested state with a glass-like state. Although the state transition has many of the characterizes of the glass transition, it would seem more suiting to denoted the transition as an active-crystallization, or the other way around, active-melting.

Further, one could also argue that the system is in a state of partially jamming for all self-propulsion velocities. The limited size of the system imposes a high packing fraction. As an effect the individual velocity of each particle is much lower than the self-propulsion velocity, even for high self-propulsion velocity where the mobility is relatively high. One could speculate that a pure jamming transition could be observed by keeping the self-propulsion velocity constant and varying the packing fraction of the system. Such phase transition due change in packing fraction has be found by Fily et al. [31].

The choice of inter-particle potentials will highly effect the behavior of the system, and thus also the phase transition. The general behaviour of systems using both Lennard-Jones potential [30] and harmonic potentials [31] produce similar phase diagrams depending on the activity and self-propulsion on the systems. However, the details, and especially the numerical values of the transition depends highly on the system parameter used. As the results presented in this thesis is not a recreation of any previous studies, it is not reasonable to expect similar overall system behaviour.

System ordering

For the system with noe particle-particle torque the time averaged order parameter $\Pi_{\upharpoonleft\downharpoonright} = 1$ from Equation (2.35) is found to be less than 0.01 with a standard deviation of approximately 0.03 for all values of the self-propulsion velocity. This means that the systems has fully random orientations throughout the whole simulation time of the system. An example is presented in Figure 4.9 which shows a snapshot from the system with u_0 at $t = 1607.25$.

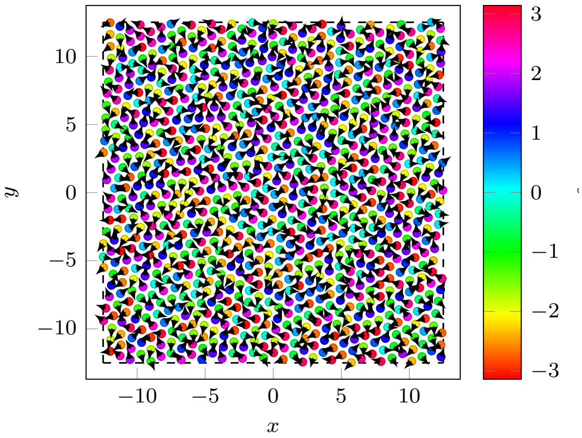

Figure 4.9: Ordering of particles of u_0 at $t = 1607.75$, corresponding to the snapshot in Figure 4.5a. The arrows and the color bar represent the orientation of each particle. The random ordering is observed for all self-propulsion velocities of the system without particle-particle torque.

In Figure 4.9 the arrows representing the orientations of the particles show no sign of ordering. The snapshot is take just before the intermittency event seen in Figure 4.5b. The orientations of the particle give no indication that an intermittency event is about to occur. The snapshot shown here is representative for all the simulations presented throughout this paragraph.

4.2.2 Simulations with particle-particle force and nematic torque

The second simulation presented will also use the parameters in Tables 4.1 and 4.2, but now with an explicit particle-particle alignment torque. The nematic flying XY-model will be used with $\gamma = 0.1$. This means that the torque Γ_{PP} in Equation (2.23) will attempt to align particles parallel or antiparallel. A non-zero alignment torque implies that the shape of the particle is elliptical. The semi-axis of the ellipse is implicitly defined by the factor γ, as discussed in Section 2.5.5.

The shape of the particle is what gives rise to the nematic particle-particle torque. Regardless of its shape, the particle has a self-propulsion velocity which gives rise to a polar orientation. For an elliptic particle this orientation lies along the major semi-axis. As in the previous section the self-propulsion velocity u_0 is varied to observe the reactions of the system.

With the nematic interactions the system is expected to have a certain degree of inter-particle ordering. To investigate this ordering for the system, the time and system averaged nematic order parameter, Equation (2.34), is plotted in Figure 4.10. The time average is averaged from $t = 0$ to the end of the simulation $t = 10000$ to include the whole transient behaviour of the system.

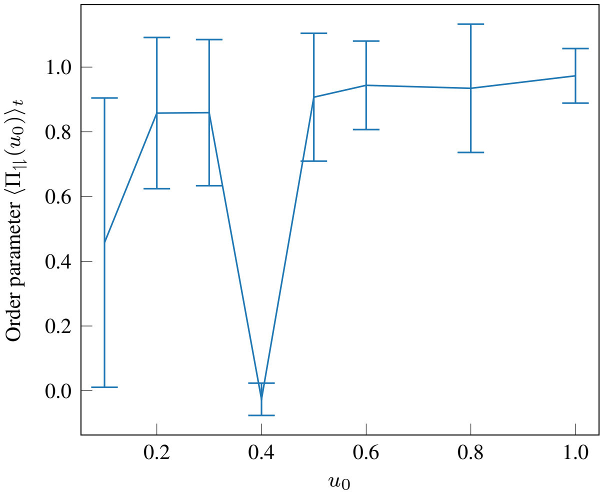

Figure 4.10: The time averaged order parameter from Equation 2.34 as a function of self-propulsion velocity u_0. The error bars represent the variance of each point. The large values of the error bars are caused by the transient behaviour of the system.

From Figure 4.10 the ordering is found to be rather high for all values of the self-propulsion velocity with exception of $u_0 = 0.4$. The error bars in the plot show the standard deviation for the time averaged ordered parameter. The values of the standard deviation does not show an intuitive scaling with neither the self-propulsion velocity nor the time averaged order parameter. As will be discussed in the results to follow, it turns out that the nematic system has a rather long transient regime before the system is relaxed into a steady state.

The first indication of the transient behaviour of the nematic system can be seen by the time-dependent nematic order parameter visualized in Figure 4.11. The self-propulsion velocities 0.1, 0.4 and 0.6 is plotted to get an example of each type of behaviour observed. Each plot in the figure is a temporal average of 40 data points which equal 10 time units. This is done to reduce the noise in the time depended plot and increase readability.

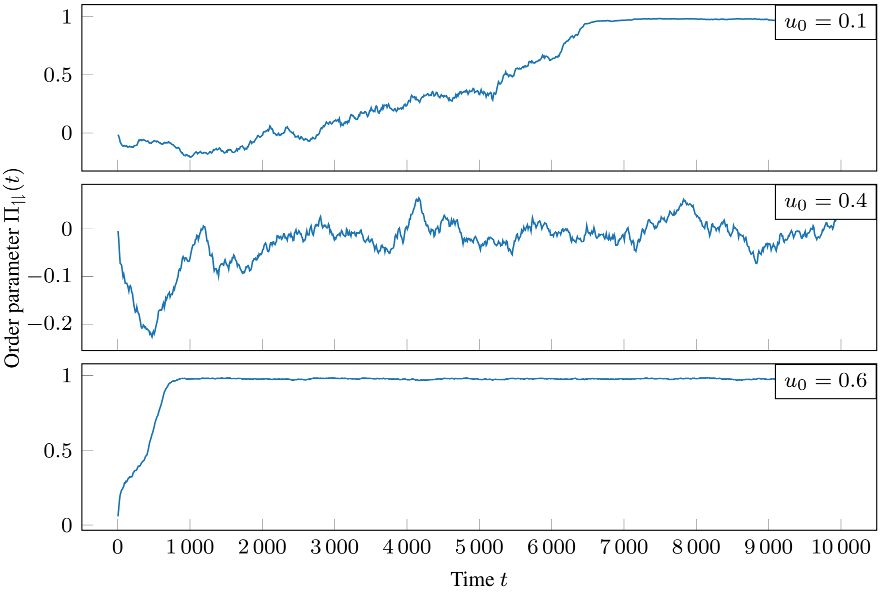

Figure 4.11: The time dependent order parameter from Equation 2.34. The different values of u_0 show different behaviour of the system. A globally ordered state is reached for $u_0 = 0.1$ and 0.6, but not for 0.4.

The top and bottom plots in Figure 4.11 show the same kind of transient behaviour. At $t = 0$ the ordering of the system start around 0, which is as expected as the particles are initialized randomly. As time passes the system gradually become more ordered until the system is fully ordered with $\Pi_{1\downarrow} = 1$. The ordering exhibits monotonic increase indicating that the process might be irreversible. As the system has relaxed into its steady state the fluctuations in the order parameter seems to vanish. The highly ordered state can therefore be assumed to be more energetically favorable to the randomly ordered state.

As clear from Figure 4.11, the top graph converges slower to 1 than the bottom graph. This is as expected since the bottom graph has a larger self-propulsion velocity. For a larger self-propulsion velocity a particle will spend more time within the cutoff radius of their neighbouring particles. Therefore, each particle will effectively have more influence on the orientation of the other particles in the system.

For further analyses of the order parameter, a characteristic length can be calculated, which measures the length scale needed for the system to reach an ordered state. The length can be defined as $u_0 t^\star$, where $t^\star$ is the time where full nematic order is reached. The characteristic lengths become approximately 650 and 435 length units for $u_0 = 0.1$ and 0.6, respectively, and for the reaming values of u_0 seen in Figure 4.10, the values range from 205 to 892, without any obvious scaling with the self-propulsion velocity. From the calculations, the characteristic length for system ordering is found to be of the same order of magnitude for all self-propulsion velocities. From this observation it is reasonable to assume that the characteristic length and therefore also characteristic time of ordering is highly system dependent and governed by the stochastic nature of the system. In order to obtain higher understanding of the ordering time, an ensemble average could be useful. This will not be the focus of this thesis.

The middle plot in Figure 4.11 shows a quite different degree of ordering than the rest of the self-propulsion velocities, including the once not visualized in the figure. The order parameter seems to oscillate around an ordering of 0. Furthermore, there are no clear signs that the order parameter is converging towards 1. Interestingly, this type of non-converging behaviour towards an ordering of $\Pi_{\uparrow\downarrow} = 1$ is only observed for $u_0 = 0.4$. An in-depth investigation of the particle orientations is required to clarify this phenomenon.

Figure 4.12 shows different configurations of the nematic system. The snapshots are from different values of the self-propulsion velocity and show examples both from the transient regime and the steady state. Together the snapshots show all the different states of the systems, although only a few self-propulsion velocities are represented.

Common for all the snapshots is the prominent parallel or antiparallel ordering of close neighbors. The local ordering is regardless of the self-propulsion velocity and evolved time in the system, implying that the nematic forces quickly overcome the initial random state. By examining the arrows in the snapshots, the orientation in a local region seem to be distributed roughly equal in each direction of the local order. Therefore the sum of the forces acting on a particle and the particle's self-propulsion force will be close to zero, and thus, the average velocity in a local area is assumed to be much smaller than the self-propulsion velocity.

Figure 4.12a is the state of the system at $t = 4000$ where the system still is in the transient regime. Here the directions of the particles can be found to vary with the positions of the particle. However, the deviation of nematic orientation is small in a localized area around each particle. This means that the system has a short ranging order that is established rather quickly. As the time progress the range of the ordering becomes longer until it covers the whole system, as seen by the snapshot in Figure 4.12b.

For $u_0 = 0.4$ a global order in the parameter $\Pi_{\uparrow\downarrow}$, defined by Equation (2.34), is never reached. However, by inspecting the snapshot in Figure 4.12c the system looks highly order, though not along any Cartesian direction. By tracking the arrowheads from one particle to another the traced path makes a circular-like curve. For instance by tracing the arrows from the center, starting by going upwards, the arrows will curve and eventually lead to the edge at $y = 12.5$. Here, because of periodic boundary condition, the path continues from the bottom of the system. The path will continue to curve until it leads back to the starting point. The shape this path creates is observable for each particle throughout the simulation of the system. Therefore, the system can be considered highly ordered, but not in terms of the order parameter $\Pi_{\uparrow\downarrow}$. A global order parameter measuring the the degree of local ordering would yield the desired result. The behaviour observed here is similar to the vortices occurring in a circular boundary system simulated by Henkes et al. [28].

Figure 4.12d shows a highly ordered state for $u_0 = 0.6$ As with the other snapshots,

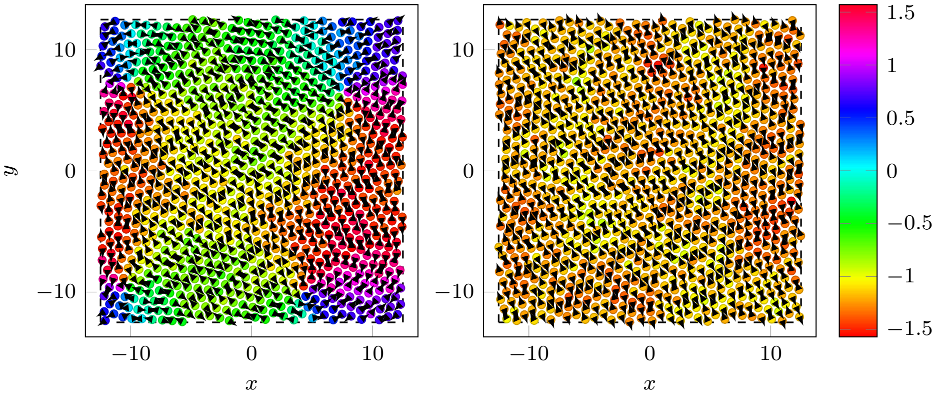

(a) $u_0 = 0.1, t = 4000.$ **(b)** $u_0 = 0.1, t = 8000.$

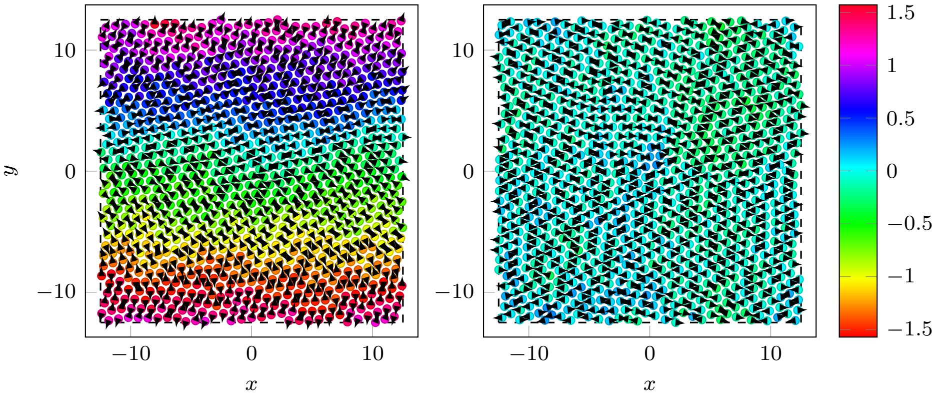

(c) $u_0 = 0.4, t = 5000.$ **(d)** $u_0 = 0.6, t = 5000.$

Figure 4.12: Particle configurations for different times and self-propulsion velocities. The arrows represent the orientation of each particle. The color bar represents the nematic orientation of of each particle, which ranges from $-\pi/2$ to $\pi/2$. The particle extent should in principle be elliptical. The scale of the particles are smaller than their actual size, in order to separate the particles from each other. (a) and (c) show local nematic ordering, while (b) and (d) show a high degree of global nematic ordering.

the particles have a tendency to match up in pairs of antiparallel alignment. The configuration of the system is almost identical to that of Figure 4.12b, except for the orientation of the global ordering. This shows that the active matter system does not have a preferred orientation in the steady state, as discussed in Section 2.7, and that the final state is dependent on the stochastic nature and initialization of the system. Moreover, this is the reason for why the system is able to find highly ordered steady state without a high value of $\Pi_{\uparrow\downarrow}$.

The histograms for the system with no particle-particle torque, presented in the previous section, gave enlightening information about the characteristics of the system. Therefore, to increase the insight of the nematic system, the histograms of system energy are presented in Figure 4.6. The self-propulsion velocities in the histograms correspond to the ones presented in Figures 4.10 and 4.12. The time interval for the histograms are $t \in [10^3, 10^4]$.

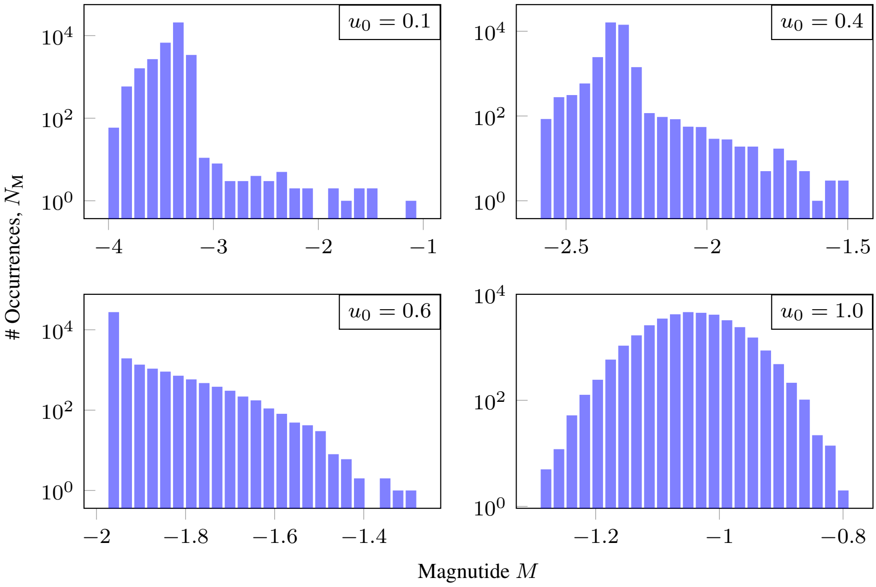

Figure 4.13: Histograms of normalized kinetic energy, Equation (2.41), in nematic systems. Selected values of the self-propulsion is plotted. The histograms are generated from the same simulations as Figure 4.12.

On initial inspection, the histograms in Figure 4.13 look rather similar to the ones in Figure 4.6. For small values of the self-propulsion velocities the energy distributions are weighted towards low energies. As the self propelling velocity increase, the distribution changes towards a parabola. As discussed in the previous section, the parabola shape is an indication of free-like particles. For highly ordered states, this is the kind of behaviour excepted, at least if the system is not in a state of dynamical arrest.

As seen from Figures 4.11 and 4.12 the systems converge to an ordered state given enough time. This argues that all the histograms should have a parabola-like distribution. However, the sampling of histograms start from $t = 1000$ which means the transient regime of the system is incorporated in the histogram. Ideally, two sets of histograms should have been presented, one for the transient regime and one for the steady state of the system. For the histograms with $u_0 = 0.1$, 0.4 and 0.6 energies many magnitudes larger than that of the steady state exists. This means that the large energy magnitudes are created in the transient regime, while the low magnitudes relate to the steady state. Therefore it is plausible that all the histograms would show parabolas if the data was sampled only from the transient regime. For $u_0 = 1.0$, the steady state is reached before $t = 1000$ and therefore the expected parabola shape is depicted.

For a further exploration of the temporal behaviour of different self-propulsion velocities, the averaged system energy, as a function of time, is plotted in Figure 4.14. The time interval $t \in [5000, 6000]$ is chosen such that some realizations of the system have reached the steady state and some have not. The energies presented are only meant to give a brief understanding of the time dependent energy and do not investigate all self-propulsion velocities in full detail. The goal is to find some general trends of the system and not a full characterization.

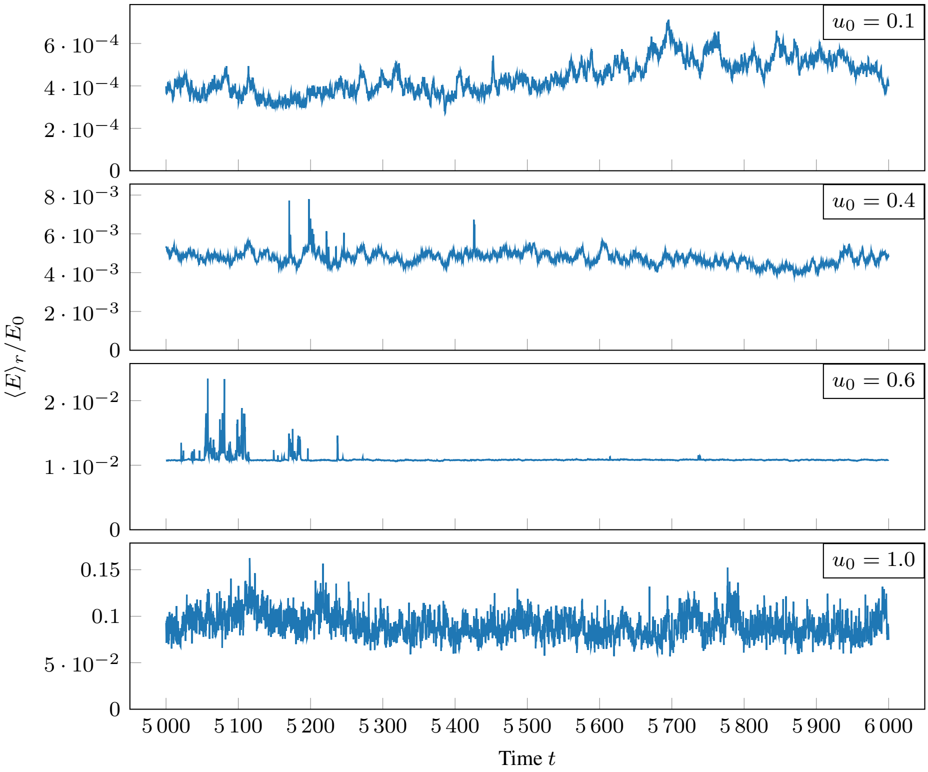

Figure 4.14: Average normalized kinetic energy as a function of time for different values of the self-propulsion velocity in nematic systems. None of the self-propulsion velocities give system-wide dynamical arrest.

For $u_0 = 0.1$ the time interval presented belongs to the transient regime. The normalized energy calculated is in general very low with small fluctuations. Outside the time interval the energy can be found to have the same behaviour. The energy plot for $u_0 = 0.4$ is very similar to 0.1. Some of the fluctuations that appear are large relative to the average energy. For $u_0 = 0.4$ previous observation indicate that system is ordered in a circular-like pattern for most of the simulation time. The energy is quite similar outside the presented interval. This means that the ordering of the system does not effect the motion of the particles for small self-propulsion velocity.

The energy for $u_0 = 0.6$ shows a more interesting behaviour. Again, the system is in the steady state. For most of the interval the system has a stable normalized energy of approximately 0.01. However, between $t = 5000$ and 5200 some spikes in the energy occur. Similar events can be seen outside the time interval presented. These events are similar to the once observed in Figures 4.4a and 4.7 for the system with no particle-particle torque. Here, these events were categorized as intermittency event seen as a slip-and-stick motion in the system. It is therefore possible to assume the ordered nematic system also may exhibit slip-and-stick motion. The main difference here, is that the particles have a non-zero energy, in what would be an analogy to the dynamical arrested state. A possible explanation is that the particles in the system are caged by its neighbours and that the ordered particles favour one direction and therefore generate a slight movement of the whole system.

As u_0 is increased to 1.0, the energy of the system looks similar to free-particle-like behaviour seen in the bottom plot in Figure 4.7. The intermittency events from $u_0 = 0.6$ is no longer visible. This system has a well-defined normalized energy average of around 0.1, with regular fluctuations. The energy behaviour seen here is typical for a liquid state, as discussed in the previous section.

In general, it seems as the both the system with no particle-particle torque and the nematic systems, has a transition for a state with dynamical arrest, or at least collective motion, to a state with significantly increased movement of the particles. The nature of the systems behave surprisingly similar taken into account that the ordering of the systems are very different. There might be many explanations for this, where one will be proposed by the author.

For the nematic system, the particles pairwise align antiparallel to a large extent. This paring will average the force on the particle and the self-propulsion velocity to approximately zero. This cancellation of the forces will also arise for a group of particles in a system with periodic boundaries where their orientation is random. This comparison explains how the nature of the two systems will become almost identical. Thus, the behaviour will only be governed by the competition between the crowding and the activity of the particles and the ordering of the system will have no or a small impact of the characteristics of the systems. In other word, the system behaviour is governed only by the ability of self-propelled particles to overcome the particle-particle interaction forces. This explanation will only hold as long the steady state of the nematic system is reached and most of the particles order in antiparallel pairs.

For all the snapshots in Figure 4.12 long range ordering across the whole system can be observed. Therefore, the nematic system breaks with the Mermin and Wagner theorem. The type of ordering and/or direction of ordering is different for all the snapshots. The ordered state of which system ends up in cannot be defined by its initial state, but is random. This can be look upon as a spontaneous symmetry break. The symmetry of the initial state is broken when the system achieves an arbitrary ordered state.

The diffusion coefficient of the system is set to a relatively small value, such that the stochastic nature of the system does not suppress the particle-particle interactions. This is probably the reason for why the system takes on a ordered state regardless of the value of the self-propulsion velocity. By increasing the diffusion coefficient of the system it is not unreasonable to expect the system to go from the ordered state to a chaotic state, much like a magnet heat above the Curie temperature, as discussed in Section 2.7.

Chapter 5

Conclusion

5.1 Current simulations and future directions

The first result of this thesis is numerical computations carried out for a highly dense, two-dimensional, active matter system. The particles in the system are governed by their self-propulsion velocity, periodic boundary conditions and linear particle-particle forces, and they have no particle-particle torques. The simulations of the active-matter system shows strong dependencies on the self-propulsion velocities of the particles.

The high packing fraction of the system leads to dynamical arrest for low self-propulsion velocities. In the dynamically arrested state the velocities of the particles are zero. An increase of the self-propulsion velocity would not necessarily lead to an increase in particle velocities, but rather an increased of self-propulsion forces, originating from each particle. As the self-propulsion forces are increased, well defined intermittency events are observed. When the self-propulsion velocity is increased sufficiently, the system-wide dynamical arrest ceases. The system is found to have a phase transition dependent on the self-propulsion velocity. This phase transition is caused as the activity, i.e. the self-propulsion force, overcomes crowding from particle-particle-interaction forces. These observations show strong similarities to the simulations by Mandal et al. [30], where hard repulsive potentials are used.

The hexagonal structuring of the particles in the systems with dynamical arrest, shows clear indications of a periodic ordering, and the state is therefore defined as an active crystal, reminiscent of the active crystals observed by Palacci et al. [10]. The intermittency events are identified from repeated short energy peaks as time progresses. The events can be observed as avalanches. At intermediate self-propulsion velocities the system reaches a critical state, where the energy distribution of the system follows the Gutenberg-Richter law. Close to the critical point, the behaviour of the four-point susceptibility function and kurtosis of the system changes.

For low values of the self-propulsion velocities the four-point susceptibility function shows diffusive behaviour for short time intervals and exhibits α-relaxation for longer time intervals. The α-relaxation is a signature of cooperative particle motion in local regions of the system. This is typical for arrested states with intermittency events. As the self-propulsion velocity is increased above the critical point, the shape of the four-point susceptibility function takes on the characteristic shape for that of a liquid. In addition the kurtosis decreases, implying that there is no longer dynamical arrest. The hexagonal structuring of the particles are still visible for the flowing state of the system, i.e. a state without dynamical arrest. For high values of self-propulsion velocity, the state of the system is identified as an active-liquid crystal. The phase transition from an active crystal to and active liquid crystal shows similarities to of the glass transition described by Toninelli et al. [1].

Berthier et al. [54] et al. defines the glass transition phenomenon as a competition between the crowding and the activity of the system, while jamming is defined as a zero-temperature and zero-activity transition, merely caused by the geometry of the system. Of these two definitions, the transition from the active crystal to the active liquid crystal is most correctly defined by the glass transition phenomenon. However, the system can also be considered partly jammed, as the high density reduces the particle velocities well below the self-propulsion velocity, regardless of the state of the system. The phase transition observed in this thesis is similar the simulations done by Fily et al. [31], Henkes et al. [28] and Mandal et al. [30]. The main difference is that these articles use binary particle mixtures, and they do not identify intermittency outside the critical regime of the system.

In the nematic active matter system, i.e. the system including the flying XY-model for the particle-particle torque, a transient regime is observed before the system transitions into an ordered state, for all the simulated values of the self-propulsion velocity. The ordered state consist of a mixture of pairs of particles aligned antiparallel and strings of particles aligned parallel. The system does not have a preferred direction or structuring of ordering, which implies that the system exhibits spontaneous symmetry breaking. The long-range ordering across the system argues that the Mermin and Wagner theorem is not upheld for such active matter systems.

The ordering of the nematic system creates a collective movement of all the particles. On top of this motion, intermittency events, similar to those observed in the system without particle-particle torque, are observed. The time dependent energy of the nematic system indicates a phase transition closely related to the transition from an active crystal to an active liquid crystal. However, the results presented for the nematic system does not give enough evidence to conclude that such a transitions takes place.

For future research it would be interesting to create a full three-dimensional phase diagram depending on the coefficient of diffusion and the coupling strength of the particle-particle torque, in addition to the self-propulsion velocity. A full characterization of the three system parameters aforementioned could increase the understanding of phase transitions in active-matter physics. The high degree of nematic ordering regardless of the self-propulsion velocities is a surprising result that demands further investigation. By extension, other types of particle-particle torque could also be of insert, such as the one used by Henkes et al. [28].

5.2 Further development of simulation tool

From a computational point of view, several improvements may be made to the simulation tool. In Chapter 3 the AB2 integration scheme was derived. By using this scheme, it is possible to achieve more precises results or decrease computational time of each simulation.

In order to simulate a higher number of particles per system, the fact that the simulation tool has a execution time that scales as $\mathcal{O}(n^2)$, should be handled. To overcome this challenge there are two potential solutions. The first one is to make the code itself more efficient. One approach is to divide the system into cells, with sizes larger than the cutoff distance for the interaction, and significantly smaller than the system size. With this solution, fewer iterations are needed to calculate neighbouring interactions.

Another solution is to parallelize the code. As the particles are dependent on previous temporal step of both its own position and neighbouring particles' position, parallelization could prove troublesome. Shared-memory systems would be ideal, as the data communication related to distributed-memory systems, would be very high. The parallelization of code does not solve the scaling issue related to an increasing number of particles, it will only decrease the computational time.

Finally, if the simulation tool is to be used by other people than the author, a proper interface should be created. At present the model parameters are saved within the core code, and a new compilation is required for each system realization. The use of Json-files or txt-files for model parameters could be a solution.

Bibliography

[1] C. Toninelli, M. Wyart, L. Berthier, G. Biroli, and J. P. Bouchaud. Dynamical susceptibility of glass formers: Contrasting the predictions of theoretical scenarios. *Physical Review E*, 71(4):041505, 2005.

[2] U. Lopez, J. Gautrais, I. D. Couzin, and G. Theraulaz. From behavioural analyses to models of collective motion in fish schools. *Interface focus*, 2(6):693–707, 2012.

[3] A. Doostmohammadi, J. Ignés-Mullol, J. M. Yeomans, and F. Sagués. Active nematics. *Nature communications*, 9(1):1–13, 2018.

[4] M Cristina Marchetti, Jean-François Joanny, Sriram Ramaswamy, Tanniemola B Liverpool, Jacques Prost, Madan Rao, and R Aditi Simha. Hydrodynamics of soft active matter. *Reviews of Modern Physics*, 85(3):1143, 2013.

[5] R. A. L. Jones. *Soft condensed matter*, volume 6. Oxford University Press, 2002.

[6] É. Fodor and M. C. Marchetti. The statistical physics of active matter: From self-catalytic colloids to living cells. *Physica A: Statistical Mechanics and its Applications*, 504:106–120, 2018.

[7] A. Bottinelli, D. T. J. Sumpter, and J. L. Silverberg. Emergent structural mechanisms for high-density collective motion inspired by human crowds. *Physical review letters*, 117(22):228301, 2016.

[8] J. K. Parrish and W. M. Hamner. Three dimensional animals groups. *Cambridge, England: Cambridge University Phys. Rev. Ess*, 1997.

[9] A. Cavagna and I. Giardina. Bird flocks as condensed matter. *Annu. Rev. Condens. Matter Phys.*, 5(1):183–207, 2014.

[10] J. Palacci, S. Sacanna, A. P. Steinberg, D. J. Pine, and P. M. Chaikin. Living crystals of light-activated colloidal surfers. *Science*, 339(6122):936–940, 2013.

[11] C. Dombrowski, L. Cisneros, S. Chatkaew, R. E. Goldstein, and J. O. Kessler. Self-concentration and large-scale coherence in bacterial dynamics. *Physical review letters*, 93(9):098103, 2004.

[12] Y. Harada, A. Noguchi, A. Kishino, and T. Yanagida. Sliding movement of single actin filaments on one-headed myosin filaments. *Nature*, 326(6115):805, 1987.

[13] Y. Y. Toyoshima, S. J. Kron, E. M. McNally, K. R. Niebling, C. Toyoshima, and J. A. Spudich. Myosin subfragment-1 is sufficient to move actin filaments in vitro. *Nature*, 328(6130):536, 1987.

[14] G. Grégoire and H. Chaté. Onset of collective and cohesive motion. *Physical review letters*, 92(2):025702, 2004.

[15] K. E. Andreassen. Active matter states of self-propelled dipolar particles. *Department of Physics, NTNU*, 2019.

[16] E. Stubberud. Ordering dynamics of active matter in circular confinement. *Department of Physics, NTNU*, 2019.

[17] T. Vicsek, A. Czirók, E. Ben-Jacob, I. Cohen, and O. Shochet. Novel type of phase transition in a system of self-driven particles. *Physical review letters*, 75(6):1226, 1995.

[18] A. P. Solon, H. Chaté, and J. Tailleur. From phase to microphase separation in flocking models: The essential role of nonequilibrium fluctuations. *Physical review letters*, 114(6):068101, 2015.

[19] D. S. Lemons and A. Gythiel. Paul langevin's 1908 paper "on the theory of brownian motion" ["sur la théorie du mouvement brownien," cr acad. sci.(paris) 146, 530–533 (1908)]. *American Journal of Physics*, 65(11):1079–1081, 1997.

[20] G. G. Stokes. On the effect of internal friction of fluids on the motion of pendulums. *Transactions of the Cambridge Philosophical Society*, 9(2):8–106, 1851.

[21] T. Brotto, J. B. Caussin, E. Lauga, and D. Bartolo. Hydrodynamics of confined active fluids. *Physical review letters*, 110(3):038101, 2013.

[22] E. M. Purcell. Life at low reynolds number. *American journal of physics*, 45(1):3–11, 1977.

[23] H. C. Berg. *Random walks in biology*. Princeton University Press, 1993.

[24] R. M. Navarro and S. M. Fielding. Clustering and phase behaviour of attractive active particles with hydrodynamics. *Soft Matter*, 11(38):7525–7546, 2015.

[25] S. Ramaswamy. The mechanics and statistics of active matter. *Annu. Rev. Condens. Matter Phys.*, 1(1):323–345, 2010.

[26] A. P. Berke, L. Turner, H. C. Berg, and E. Lauga. Hydrodynamic attraction of swimming microorganisms by surfaces. *Physical Review Letters*, 101(3):038102, 2008.

[27] A. P. Solon, Y. Fily, A. Baskaran, M. E. Cates, Y. Kafri, M. Kardar, and J. Tailleur. Pressure is not a state function for generic active fluids. *Nature Physics*, 11(8):673, 2015.

[28] S. Henkes, Y. Fily, and M. C. Marchetti. Active jamming: Self-propelled soft particles at high density. *Physical Review E*, 84(4):040301, 2011.

[29] F. D. C. Farrell, M. C. Marchetti, D. Marenduzzo, and J. Tailleur. Pattern formation in self-propelled particles with density-dependent motility. *Physical review letters*, 108(24):248101, 2012.

[30] R. Mandal, P. J. Bhuyan, P. Chaudhuri, C. Dasgupta, and M. Rao. Extreme active matter at high densities. *Nature Communications*, 11(1):1–8, 2020.

[31] Y. Fily, S. Henkes, and M. C. Marchetti. Freezing and phase separation of self-propelled disks. *Soft matter*, 10(13):2132–2140, 2014.

[32] M. R. Shaebani, A. Wysocki, R. G. Winkler, G. Gompper, and H. Rieger. Computational models for active matter. *Nature Reviews Physics*, pages 1–19, 2020.

[33] D. Chandler, J. D. Weeks, and H. C. Andersen. Van der waals picture of liquids, solids, and phase transformations. *Science*, 220(4599):787–794, 1983.

[34] J.E. Lennard-Jones. On the determination of molecular fields. ii. from the equation of state of a gas. *Proceedings of the Royal Society of London. Series A, Containing Papers of a Mathematical and Physical Character*, 106(738):463–477, 1924.

[35] D. M. Heyes and H. Okumura. Equation of state and structural properties of the weeks-chandler-andersen fluid. *The Journal of chemical physics*, 124(16):164507, 2006.

[36] H. H. Kausch, D. G. Fesko, and N. W. Tschoegl. The random packing of circles in a plane. *Journal of Colloid and Interface Science*, 37(3):603–611, 1971.

[37] M. C. Bott, F. Winterhalter, M. Marechal, A. Sharma, J. M. Brader, and R. Wittmann. Isotropic-nematic transition of self-propelled rods in three dimensions. *Physical Review E*, 98(1):012601, 2018.

[38] V. A. Miransky. *Dynamical symmetry breaking in quantum field theories*. World Scientific, 1993.

[39] N. D. Mermin and H. Wagner. Absence of ferromagnetism or antiferromagnetism in one-or two-dimensional isotropic heisenberg models. *Physical Review Letters*, 17(22):1133, 1966.

[40] J. Toner and Y. Tu. Long-range order in a two-dimensional dynamical xy model: how birds fly together. *Physical review letters*, 75(23):4326, 1995.

[41] J. Toner and Y. Tu. Flocks, herds, and schools: A quantitative theory of flocking. *Physical review E*, 58(4):4828, 1998.

[42] O. Dauchot, G. Marty, and G. Biroli. Dynamical heterogeneity close to the jamming transition in a sheared granular material. *Physical review letters*, 95(26):265701, 2005.

[43] A. S. Keys, A. R. Abate, S. C. Glotzer, and D. J. Durian. Measurement of growing dynamical length scales and prediction of the jamming transition in a granular material. *Nature physics*, 3(4):260–264, 2007.

[44] A. R. Abate and D. J. Durian. Topological persistence and dynamical heterogeneities near jamming. *Physical Review E*, 76(2):021306, 2007.

[45] K. N. Nordstrom, J. P. Gollub, and D. J. Durian. Dynamical heterogeneity in soft-particle suspensions under shear. *Physical Review E*, 84(2):021403, 2011.

[46] H. Kang, T. R. Kirkpatrick, and D. Thirumalai. Manifestation of random first-order transition theory in wigner glasses. *Physical Review E*, 88(4):042308, 2013.

[47] G. Szamel and E. Flenner. Four-point susceptibility of a glass-forming binary mixture: Brownian dynamics. *Physical Review E*, 74(2):021507, 2006.

[48] G. D. Smith and D. Bedrov. Relationship between the α-and β-relaxation processes in amorphous polymers: Insight from atomistic molecular dynamics simulations of 1, 4-polybutadiene melts and blends. *Journal of Polymer Science Part B: Polymer Physics*, 45(6):627–643, 2007.

[49] E. R. Weeks, J. C. Crocker, A. C. Levitt, A. Schofield, and D. A. Weitz. Three-dimensional direct imaging of structural relaxation near the colloidal glass transition. *Science*, 287(5453):627–631, 2000.

[50] J. P. Sethna, K. A. Dahmen, and C. R. Myers. Crackling noise. *Nature*, 410(6825):242–250, 2001.

[51] B. Gutenberg and CF Richter. Frequency and energy of earthquakes. *Seismicity of the Earth and Associated Phenomena*, pages 17–19, 1954.

[52] P. A. Houle and J. P. Sethna. Acoustic emission from crumpling paper. *Physical Review E*, 54(1):278, 1996.

[53] J. P. Sethna, K. A. Dahmen, S. Kartha, J. A. Krumhansl, B. W. Roberts, and J. D. Shore. Hysteresis and hierarchies: Dynamics of disorder-driven first-order phase transformations. *Physical Review Letters*, 70(21):3347, 1993.

[54] L. Berthier, E. Flenner, and G. Szamel. Glassy dynamics in dense systems of active particles. *The Journal of chemical physics*, 150(20):200901, 2019.

[55] L. Berthier and M. D. Ediger. Facets of glass physics. *arXiv preprint arXiv:1512.03540*, 2015.

[56] Zhengdong Cheng, Jixiang Zhu, Paul M Chaikin, See-Eng Phan, and William B Russel. Nature of the divergence in low shear viscosity of colloidal hard-sphere dispersions. *Physical Review E*, 65(4):041405, 2002.

[57] C Austen Angell. Formation of glasses from liquids and biopolymers. *Science*, 267(5206):1924–1935, 1995.

[58] T. E. Angelini, E. Hannezo, X. Trepat, M. Marquez, J. J. Fredberg, and D. A. Weitz. Glass-like dynamics of collective cell migration. *Proceedings of the National Academy of Sciences*, 108(12):4714–4719, 2011.

[59] A. Mongera, P. Rowghanian, H. J. Gustafson, E. Shelton, D. A. Kealhofer, E. K. Carn, F. Serwane, A. A. Lucio, J. Giammona, and O. Campàs. A fluid-to-solid jamming transition underlies vertebrate body axis elongation. *Nature*, 561(7723):401–405, 2018.

[60] D. Bi, X. Yang, M. C. Marchetti, and M. L. Manning. Motility-driven glass and jamming transitions in biological tissues. *Physical Review X*, 6(2):021011, 2016.

[61] A. Haeger, M. Krause, K. Wolf, and P. Friedl. Cell jamming: collective invasion of mesenchymal tumor cells imposed by tissue confinement. *Biochimica et Biophysica Acta (BBA)-General Subjects*, 1840(8):2386–2395, 2014.

[62] S. Garcia, E. Hannezo, J. Elgeti, J. F. Joanny, P. Silberzan, and N. S. Gov. Physics of active jamming during collective cellular motion in a monolayer. *Proceedings of the National Academy of Sciences*, 112(50):15314–15319, 2015.

[63] V. Narayan, S. Ramaswamy, and N. Menon. Long-lived giant number fluctuations in a swarming granular nematic. *Science*, 317(5834):105–108, 2007.

[64] Edward Ott. *Chaos in dynamical systems*. Cambridge university press, 2002.

[65] C. J. O. Reichhardt and C. Reichhardt. Avalanche dynamics for active matter in heterogeneous media. *New Journal of Physics*, 20(2):025002, 2018.

[66] M. C. Miguel, A. Vespignani, S. Zapperi, J. Weiss, and J. R. Grasso. Intermittent dislocation flow in viscoplastic deformation. *Nature*, 410(6829):667–671, 2001.

[67] K. M. Salerno, C. E. Maloney, and M. O. Robbins. Avalanches in strained amorphous solids: does inertia destroy critical behavior? *Physical Review Letters*, 109(10):105703, 2012.

[68] A. J. Liu and S. R. Nagel. Jamming is not just cool any more. *Nature*, 396(6706):21–22, 1998.

[69] G. Maruyama. Continuous markov processes and stochastic equations. *Rendiconti del Circolo Matematico di Palermo*, 4(1):48–90, 1955.

[70] F. Balboa Usabiaga, B. Delmotte, and A. Donev. Brownian dynamics of confined suspensions of active microrollers. *The Journal of chemical physics*, 146(13):134104, 2017.

[71] B. Ewald. Weak versions of stochastic adams-bashforth and semi-implicit leapfrog schemes for sdes. *Comput. Methods Appl. Math.*, 12(1):23–31, 2012.

[72] L. Verlet. Computer” experiments” on classical fluids. i. thermodynamical properties of lennard-jones molecules. *Physical review*, 159(1):98, 1967.

[73] R. Grossmann, L. Schimansky-Geier, and P. Romanczuk. Active brownian particles with velocity-alignment and active fluctuations. *New Journal of Physics*, 14(7):073033, 2012.

[74] S. Henkes, M. C. Marchetti, and R. Sknepnek. Dynamical patterns in nematic active matter on a sphere. *Physical Review E*, 97(4):042605, 2018.

[75] S. Weitz, A. Deutsch, and F. Peruani. Self-propelled rods exhibit a phase-separated state characterized by the presence of active stresses and the ejection of polar clusters. *Physical Review E*, 92(1):012322, 2015.

[76] M. Galassi, J. Davies, J. Theiler, B. Gough, G. Jungman, P. Alken, M. Booth, F. Rossi, and R. Ulerich. *GNU scientific library*. Network Theory Limited, 2002.

[77] M. Matsumoto and T. Nishimura. Mersenne twister: a 623-dimensionally equidistributed uniform pseudo-random number generator. *ACM Transactions on Modeling and Computer Simulation (TOMACS)*, 8(1):3–30, 1998.

[78] S. van der Walt, S. C. Colbert, and G. Varoquaux. The numpy array: a structure for efficient numerical computation. *Computing in Science & Engineering*, 13(2):22–30, 2011.

[79] J. D. Hunter. Matplotlib: A 2d graphics environment. *Computing in Science & Engineering*, 9(3):90–95, 2007.

[80] Christian Feuersänger. Manual for package pgfplots. 17, 2011.

[81] The HDF Group. Hierarchical Data Format, version 5, 1997-2020. http://www.hdfgroup.org/HDF5/.

[82] P. C. Hohenberg and B. I. Halperin. Theory of dynamic critical phenomena. *Reviews of Modern Physics*, 49(3):435, 1977.

[83] J. U. Klamser, S. C. Kapfer, and W. Krauth. Thermodynamic phases in two-dimensional active matter. *Nature communications*, 9(1):1–8, 2018.

[84] Walter Kob and Hans C Andersen. Scaling behavior in the β-relaxation regime of a supercooled lennard-jones mixture. *Physical review letters*, 73(10):1376, 1994.

[85] F. Ginot, A. Solon, Y. Kafri, C. Ybert, J. Tailleur, and C. Cottin-Bizonne. Sedimentation of self-propelled janus colloids: polarization and pressure. *New Journal of Physics*, 20(11):115001, 2018.

[86] J. T. Kuhr, J. Blaschke, F. Rühle, and H. Stark. Collective sedimentation of squirmers under gravity. *Soft matter*, 13(41):7548–7555, 2017.

Appendix A

Validation of simulation program

A.1 Optimization of time steps for integration schemes

In the simulation program the time step have to be optimize to ensure that the particles interact as the should. If the time steps is too large, the particles may move too far into the potential of neighbouring particles and exhibit non-physical behaviour or even pass right through. Therefore, an effort has been made to find a minimum requirement of the time step.

In Figure A.1 the precision of consecutive decades of time step have be benchmarked against each other. The approach is as follows: First a a periodic boundary system is simulated with no diffusion for a given time step. Then another simulation is run for the exact same initial conditions, but now in a time step 10 times smaller. The two simulations are compared by looking at the difference in each particle of the system between the two simulations. The proses is repeated for three sets of time steps and for both the Euler-Maruyama and Adams-Bashforth integration scheme.

From the plot it is apparent that the error related to the position of the particles will gradually increase with time, regardless of how small the time step is. As a results of this, it seems as if both EM and AB2 will never find a state with a precision lower than a certain threshold after enough time has passed. This motivates another approach for optimizing the time-stepping, namely quantizing the time step limit for non-physical behaviour. A type of non-physical behaviour in this active matter system may be a dramatic change in velocity, which becomes much larger than the self propelled velocity. In such a scenario the the change in position of the particle for a single time step can be many orders of magnitude larger than the system size. This motivates further exploration of the behaviour of the system rather than the precision of the integration schemes. One example is looking at the sedimentation of a free particle in a well.

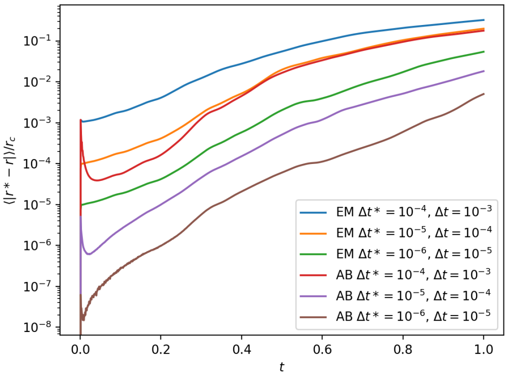

Figure A.1: Comparison of position between two time steps as a function of time for EM and AB2. The system is simulated for 1000 particles with with no rotational diffusion, i.e. $D_r = 0$. Initially, the particles are distributed homogeneously inside the boundary.The self-propelling velocity of the particles is $u_0 = 10.0$.

A.2 Sedimentation in infinite potential well

In order to test the numerical implementation, a comparison to an active system with an analytical solution is presented. For an active system subject to a gravitational force, the particles will sediment in the direction of the gravitational field. In the framework descried in Chapter 2 the gravitational potential gives the particle a constant gravitational velocity or sedimentation velocity v_s, analogous to the self-propelling velocity v_0. As previously stated, the viscous drag forces essentially makes all other forces cancel out which leads to a constant velocity induced by the gravitational potential. The equation of motion in Equation 2.6 will now take the follow form,

$$\frac{d\vec{r}(t)}{dt} = v_0 \vec{u}(t) - v_s \hat{e}_z. \tag{A.1}$$

The other equations governing the behaviour of the particle, i.e. Equations 2.7 and 2.8 remain unchanged.

For a simple system without particle-particle interaction where the sedimentation velocity v_s is much smaller than the self-propelling velocity v_0 the system, which behaves as an equilibrium system [85], can be described by,

$$\rho(z) \propto \exp -(mgz/kT_{\text{eff}}). \tag{A.2}$$

The effective temperature is given by the Stokes-Einstein relation $kT_{\text{eff}} \equiv D/\mu$, where D is the diffusion constant and μ is the motility of the system.

The Fokker-Planck equation can be used to derive the position $\vec{r}$ and orientation θ of the a particle governed by Equation (A.1). Following, the density profile can be shown to tale the from $\rho(z) \propto \exp(-z/\lambda)$, with a sedimentation length λ. For small v_s/v_0 the sedimentation length is described by the expansion [85],

$$\lambda = \frac{v_0^2}{2D_r v_s}\left[1 - \frac{7}{4}\left(\frac{v_s}{v_0}\right)^2 + \mathcal{O}\left(\left(\frac{v_s}{v_0}\right)^4\right)\right]. \tag{A.3}$$

I the limit $v_s/v_0 << 1$, λ should equal kT_{eff}/mg, such that Equations (A.2) and (A.3) converges toward the same value.

A.2.1 Simulations of particle sedimentation

In the previous section, the analytical expression for the density, and therefore also the probability distribution of the sedemnatition of an active matter system was derived. Here, this solution can be used to validate the implementation of the simulation program.

To achieve relevant comparisons between the simulations and the analytical solutions, many approaches can be used. A rather simple approach, is to simulate a two dimensional, infinitely high well, where the gravitational force act towards the bottom of the well. In such a system, the particle will have a free-particle-like behaviour only affected by the gravitational potential and the system boundary. In such a system the particles should have an exponential density distribution.

The density distribution of the system can be found be simulating a single particle, and sampling the position of the particle at regular time intervals. Figure A.2a presents the sampling of the y position of a well confined by the infinitely high potential. As seen from the histogram in Figure A.2b the distribution yield an exponential shape, as would be expected. The results of the histogram are normalized to achieve a probability distribution rather than a sample count. This allows for comparison between the numerical results and the λ-value in Equation A.3.

From the numerical data, two approaches can be used to find the sedimentation length of the simulation. The first one is a simple linear regression of the logarithmic values of the histogram. The second approach, and perhaps a more precise method, is the use maximum likelihood estimation on the position sampling itself. For an exponential distribution of the from $\kappa \exp\left(-z/\kappa\right)$ the maximum likelihood estimation for κ is

$$\hat{\kappa} = \frac{n}{\sum_{i=1}^{n} z_i}. \tag{A.4}$$

Here n is the number of sampling points. The estimator $\hat{\kappa}$ is the reciprocal of the average position. Figure A.3 shows the linear regression and the maximum likelihood estimation together with the analytical value of the sedimentation length as gradients. The standard error for the linear regression is 0.001006 and for the maximum likelihood estimation it is 0.000049.

Figure A.3 shows a great fit between analytical solution and both the maximum likelihood estimator and the linear regression. If the tail of the distribution, which contains very few data points, was omitted, the fits would be even better. These results are similar to the ones in the studies by Ginot et al. [85] and Kuhr et al. [86]. This is clear argument that the simulation presented exhibits the expected behaviour. The simulation uses $u_0 = 10.0$ and $\Delta t = 0.001$, where as the rest of this thesis has a maximum of $u_0 = 1.0$. As the time step is directly dependent on the system velocity, it is not unreasonable to use $\Delta t = 0.01$ for $u_0 = 1.0$. However, for safe measures, a time step $\Delta t = 0.005$ will be used in this thesis.

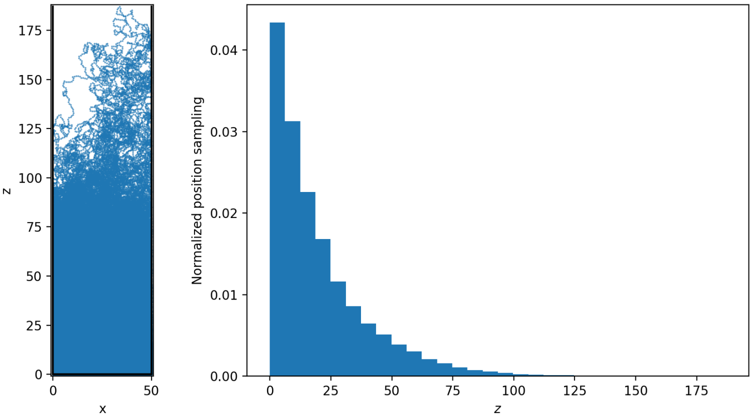

(a) Position sampling **(b)** Histogram of sampling

Figure A.2: Figure (a) shows sampling data of the position for a single particle, and (b) shows the corresponding histogram of the y positions. The boundaries of the well are harmonic with at width of 50. The following parameters has the values, $v_s = 0.5$, $v_0 = 10$, $D_r = 0.001$ and $\Delta t = 0.001$. The simulation is run for 10^8 steps, and the y position is sampled every 1000 step.

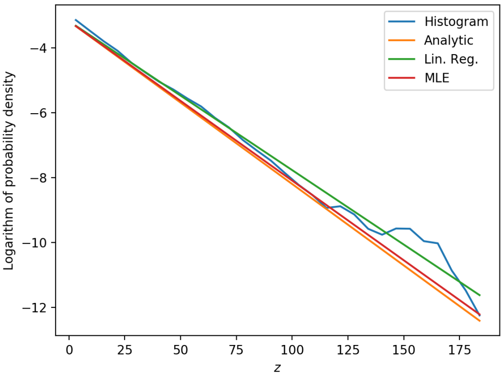

Figure A.3: Shows different estimations of the sedimentation length of the exponential distribution function. The colored lines represent the following: Blue, the logarithmic values of the histogram in Figure A.2b. Orange, the analytical sedimentation length from Equation A.3. Green, a linear regression of the blue line. Red, the exponential maximum likelihood estimator for the sample data of y. Same simulation parameters as Figure A.2

NTNU
Norwegian University of
Science and Technology